

1 **Ammonia emissions and depositions over the contiguous United States derived**
2 **from IASI and CrIS using the directional derivative approach**

3 Zitong Li^{1,2}, Kang Sun^{3,4*}, Kaiyu Guan^{1,2,5,6*}, Sheng Wang^{1,2}, Bin Peng^{1,2,5,7}, Lieven Clarisse⁸,
4 Martin Van Damme^{8,9}, Pierre-François Coheur⁹, Karen Cady-Pereira¹⁰, Mark W. Shephard¹¹,
5 Mark Zondlo¹², Daniel Moore¹²

6 ¹Agroecosystem Sustainability Center, Institute for Sustainability, Energy, and Environment,
7 University of Illinois Urbana-Champaign, Urbana, IL, USA.

8 ²Department of Natural Resources and Environmental Sciences, College of Agricultural,
9 Consumer and Environmental Sciences, University of Illinois Urbana-Champaign, Urbana, IL,
10 USA.

11 ³Department of Civil, Structural and Environmental Engineering, University at Buffalo, Buffalo,
12 NY, USA.

13 ⁴Research and Education in Energy, Environment and Water Institute, University at Buffalo,
14 Buffalo, NY, USA.

15 ⁵National Center for Supercomputing Applications, University of Illinois Urbana-Champaign,
16 Urbana, IL, USA.

17 ⁶Department of Computer Science, University of Illinois Urbana-Champaign, Urbana, IL, USA.

18 ⁷Department of Crop Sciences, University of Illinois Urbana-Champaign, Urbana, IL, USA.

19 ⁸Université libre de Bruxelles (ULB), BLU-ULB research Center, Spectroscopy, Quantum
20 Chemistry and Atmospheric Remote Sensing (SQUARES), Brussels, Belgium

21 ⁹Royal Belgian Institute for Space Aeronomy (BIRA-IASB), Brussels, Belgium.

22 ¹⁰Atmospheric and Environmental Research, Lexington, MA, USA.

23 ¹¹Environment and Climate Change Canada, Toronto, ON, Canada.

24 ¹²Department of Civil and Environmental Engineering, Princeton University, Princeton, NJ,
25 USA.

26 Corresponding authors: Kang Sun (kangsun@buffalo.edu), Kaiyu Guan (kaiyug@illinois.edu)

27

28 **Abstract**

29 Atmospheric ammonia (NH₃), primarily emitted from agriculture, poses
30 significant threats to ecosystems, climate, and human health through nitrogen
31 deposition and secondary aerosol formation. NH₃ flux estimates remain highly
32 uncertain due to limited direct observations and complex emission–deposition
33 processes. Here, we estimated NH₃ fluxes over the contiguous United States using
34 satellite observations from the Infrared Atmospheric Sounding Interferometer (IASI,
35 2008–2022) and Cross-track Infrared Sounder (CrIS, 2012–2022). ~~By~~ By applying a
36 directional derivative approach, ~~we minimized the impact of offsets in satellite-derived~~
37 ~~vertical column densities~~. Our results highlight major agricultural emission hotspots,
38 including the San Joaquin Valley in California, the Snake River Valley in Idaho, the
39 Texas panhandle, the Great Plains, Southeastern Pennsylvania, and Eastern North

40 Carolina. NH₃ removal ~~was~~ predominantly driven by deposition near source areas
41 rather than chemical transformation, with strong sinks in vegetation-dense regions
42 such as forests, grasslands, shrublands, and wetlands. Seasonal flux variations
43 showed peaks in warm months and lower values in winter, driven by temperature-
44 dependent volatilization from livestock production and fertilizer application. Compared
45 with bottom-up inventory, Satellite-based estimates aligned well with bottom-up
46 inventories, effectively capturing general spatial and seasonal patterns, while also
47 revealing additional insights into key flux hotspots and peak periods seasons. CrIS
48 consistently report see higher fluxes than IASI, especially in spring, reflecting
49 differences in their overpass times. Combining IASI (morning overpass) and CrIS
50 (midday overpass) observations enables a better understanding of diurnal NH₃ flux
51 dynamics. These findings provide critical insights into NH₃ spatiotemporal variabilities,
52 complementing inventory-based approaches and informing nitrogen management and
53 environmental policy, particularly in regions with limited ground-based monitoring.

54 1. Introduction

55 Atmospheric NH₃ is the most abundant alkaline gas (Asman et al., 1998; Sutton
56 et al., 2020), and a major component of reactive nitrogen (Galloway et al., 2004). It is
57 removed primarily through two pathways: deposition and chemical transformation.
58 Deposition occurs when atmospheric NH₃ is taken up by surfaces via dry or wet
59 processes near its emission sources. Chemical removal involves reactions with sulfuric,
60 nitric, and hydrochloric acids (Loubet et al., 2009), forming particulate ammonium
61 (NH₄⁺) and secondary pollutants (Behera and Sharma, 2010; Wang et al., 2015).
62 Global NH₃ emissions have more than doubled since pre-industrial times (Galloway et
63 al., 2003), driving a cascade of environmental consequences. NH₃ deposition and its
64 secondary chemical products contribute to ecosystem eutrophication and soil
65 acidification, disrupting natural nutrient cycles and reducing biodiversity (van Breemen
66 et al., 1982; Heil and Diemont, 1983; Sutton et al., 2008). These processes degrade
67 air quality, threaten human health (Ma et al., 2021), and influence climate through
68 radiative forcing alterations (Erisman et al., 2013; Gong et al., 2024).

69 NH₃ is emitted from various sources, including domestic animals (40%),
70 synthetic fertilizers (17%), biomass burning (11%), natural sources (19%), crops (7%)
71 and humans and pets (5%) (Bouwman et al., 1997). However, large-scale ground-
72 based measurements of NH₃ emissions are sparse due to the challenges associated
73 with accurately capturing gaseous NH₃. Observations of NH₃ fluxes are further
74 constrained by its sharp spatial gradients and short tropospheric lifetime, typically less
75 than 24 of only a few hours (Adams et al., 2019; Wang et al., 2023). Regional and
76 global NH₃ fluxes are often estimated using bottom-up approaches that rely on
77 emission factors and spatial allocation of NH₃-emitting activities (Liu et al., 2022).
78 However, these estimates have large uncertainties, reaching up to 50% (Bouwman et
79 al., 1997). A major source of uncertainty is the lack of reliable statistics on fertilizer use
80 and animal waste production. Regional variations in agricultural practices complicate
81 scaling local observations to global estimates (Luo et al., 2022). Further challenges

82 arise from limited understanding of emissions from natural sources and biomass
83 burning (Dentener and Crutzen, 1994) and the dependence of NH₃ volatilization on
84 environmental conditions ([Sommer et al., 1991](#))([Vira et al., 2022](#)).

85 Advances in satellite-based atmospheric retrievals have introduced powerful
86 tools for estimating trace gas fluxes, enabling large-scale investigation of gas
87 dynamics. For example, the Infrared Atmospheric Sounding Interferometer (IASI) and
88 the Cross-track Infrared Sounder (CrIS) have identified large NH₃ point sources
89 worldwide that were absent from bottom-up inventories (Van Damme et al., 2018;
90 Dammers et al., 2019). Chemical transport models (CTMs) have been widely
91 employed to derive gas fluxes from satellite observations (Cao et al., 2020, 2022; Chen
92 et al., 2021; Marais et al., 2021). However, the computational demands of running
93 CTMs at fine temporal and spatial scales pose significant limitations to fully leverage
94 the coverage and resolutions of new-generation satellite products. To complement
95 CTMs, observational-data-driven approaches have been developed to derive gas
96 emissions directly from satellite Level 2 products. The flux divergence method, for
97 example, has been used to estimate NO_x fluxes (Beirle et al., 2019, 2021). Closely
98 related to the flux divergence method, the directional derivative approach ([DDA](#))
99 estimates fluxes with additional agility ([Ayazpour et al., 2025](#))([Ayazpour et al., 2024](#);
100 Sun, 2022) and demonstrates broad applicability across various atmospheric species
101 and regions (Lonsdale and Sun, 2023).

102 In this study, we applied the ~~DDA~~[directional derivative approach](#) to estimate
103 NH₃ fluxes across the contiguous United States (CONUS). [We derived top-down NH₃
104 fluxes at 0.1° resolution using observations from two space-based instruments: the
105 Infrared Atmospheric Sounding Interferometer \(IASI\) and the Cross-track Infrared
106 Sounder \(CrIS\)](#)~~We used~~[Using observations from two space-based instruments, the
107 Infrared Atmospheric Sounding Interferometer \(IASI\) and the Cross-track Infrared
108 Sounder \(CrIS\), to derive top-down NH₃ fluxes at fine spatial \(0.1° grid\) and
109 temporal \(daily\) resolutions.](#) This study addresses the following questions: 1) How
110 accurately can satellite observations from IASI and CrIS be used to estimate NH₃
111 fluxes? 2) What are the spatiotemporal patterns of NH₃ fluxes over the CONUS? Our
112 findings aim to enhance the understanding of reactive nitrogen cycling and provide
113 valuable information for environmental and policy applications.

114 2. Data and Methods

115 2.1 Data

116 IASI and CrIS datasets use distinct retrieval approaches, providing two
117 independent datasets and complementary perspectives for analyzing NH₃ flux patterns.
118 IASI onboard the Metop-A/B/C meteorological payload was launched by the European
119 Organisation for the Exploitation of Meteorological Satellites (EUMETSAT), ~~starting in~~
120 [October 2006](#). Operating in a polar orbit, IASI provides global coverage with two
121 overpass times daily, morning (09:30 local solar time, LST) and at night (21:30 LST).
122 The instrument features a circular footprint on ground of 12 km along the satellite track
123 and a swath width of 2200 km ($\pm 48.3^\circ$) (Clerbaux et al., 2009). IASI measurements

124 generate vertical column densities (VCDs) of NH₃ using machine learning-based
125 retrieval algorithms. We utilized daytime (09:30 LST) NH₃ VCD measurements over
126 the CONUS from January 2008 to December 2022. The data was sourced from the
127 Level 2 reanalysis product of the ANNI-NH₃-v4R dataset (Clarisse et al., 2023) [from](#)
128 [Metop-A \(January 2008 to October 2021\), Metop-B \(March 2013 to December 2022\)](#)
129 [and Metop-C \(September 2019 to December 2022\)](#). Additionally, we excluded Metop-
130 A data after 2019 due to a drift in Metop-A's overpass time towards the end of its
131 operational life. CrIS is onboard the Suomi-NPP, NOAA-20 and NOAA-21 satellites,
132 [with the first instrument launched in October 2014](#). It also operates in a polar orbit with
133 two overpass times daily, early afternoon (13:30 LST) and after midnight (01:30 LST).
134 CrIS features a swath width identical to IASI (2200 km) and a similar ground pixel
135 resolution (14 km circular pixels at nadir). NH₃ VCDs are generated using the fast
136 physical retrieval (CFPR) approach (Shephard and Cady-Pereira, 2015; Shephard et
137 al., 2020). We used daytime (13:30 LST) NH₃ VCDs measured by CrIS-NPP [\(June](#)
138 [2012 to May 2021\)](#) and CrIS-NOAA-20 [\(March 2019 to December 2022\)](#) over the
139 CONUS for the period from June 2012 to December 2022. The dataset was derived
140 from the Level 2 CrIS NH₃ version 1.6.4 product.

141 We used gridded monthly NH₃ emission inventories from the Harmonized
142 Emissions Component (HEMCO) 3.0 for 2016- with a spatial resolution of 0.1° (Lin et
143 al., 2021). HEMCO converts publicly available emissions data, such as SMOKE
144 outputs, into inputs compatible with atmospheric models like GEOS-Chem. The
145 inventory integrates data from the National Emissions Inventory ~~(NEI)~~ and includes
146 key NH₃ sources such as agriculture, industry, and natural emissions. [We use this](#)
147 [bottom-up inventory from HEMCO to compare with Comparing these bottom-up](#)
148 [inventories estimates with](#) satellite-derived fluxes, [providing](#) insights into their
149 consistency and [helping to](#) assess the utility of satellite-based estimates.

150 ~~We This study~~ also incorporated additional datasets to support NH₃ flux
151 estimation and analysis. Hourly horizontal wind data at 100 and 10 m above the
152 surface was utilized to estimate NH₃ fluxes from [satellite VCD](#) observations. The data
153 was obtained from the ERA5 reanalysis at a spatial resolution of 0.25° (Hersbach et
154 al., 2020) spanning 2008 to 2022. The 2021 release of the National Land Cover
155 Database (NLCD) with a resolution of 30 meters was used to analyze the spatial
156 patterns of NH₃ fluxes across different land cover types. Land and water mask data
157 from the North American Land Data Assimilation System (NLDAS) unified mask were
158 used to exclude water body data due to the larger noise of the satellite retrievals over
159 these areas.

160 2.2 NH₃ flux estimations

161 2.2.1 Directional derivative approach [\(DDA\)](#)

162 The ~~estimation derivation~~ of emissions (E) from satellite-observed [VCDs column](#)
163 [amounts](#) (Ω) is grounded in the principle of mass conservation as in Eq. ~~(1)~~, [which is](#)
164 [in the same form as presented in the previous DDA literature \(Sun, 2022; Ayazpour et](#)
165 [al., 2025\)](#). [DDA accounts for horizontal transport, topographic effects, and chemical](#)

166 transformation influencing gas distribution. Three estimators within the DDA
 167 framework are labeled in Eq. 1 as DD , DD_{topo} , and DD_{chem} , representing the
 168 directional derivative of column densities, the directional derivative with consideration
 169 of topography, and the directional derivative with consideration of both topography and
 170 chemistry. ~~DDA~~This approach considers the physical and chemical processes
 171 affecting gas distribution, incorporating horizontal transport, topography, and chemical
 172 transformation. The ~~directional derivative estimator~~ first term (DD) estimator ($\vec{u} \cdot (\nabla \Omega)$)
 173 captures the ~~horizontal advection of role of wind in transporting~~ NH_3 horizontally,
 174 representing the directional derivatives of the ~~VCD~~ column amounts (Ω) with respect
 175 to horizontal wind vectors ~~representing the planetary boundary layer~~ (\vec{u} , 100 m winds
 176 ~~sampled from ERA5~~) within the planetary boundary layer. $\nabla = (\partial/\partial x, \partial/\partial y)$ is the
 177 horizontal vector differential operator. Ayazpour et al. (2025) evaluated DD estimators
 178 calculated using column amounts and winds at a range of altitudes in an atmospheric
 179 model with the model-ingested emission and found that winds from 100-800 m give
 180 similar and consistent results. We choose 100 m wind because it has been widely used
 181 in previous studies (Goldberg et al., 2022; Lonsdale and Sun, 2023) and is readily
 182 available from the ERA5 single-level product. The DD_{topo} estimator second term
 183 accounts for the topography term ($X\Omega\vec{u}_0 \cdot (\nabla z_0)$), which is driven by the directional
 184 derivatives of the surface altitudes (z_0 , obtained from Level 2 satellite data) relative to
 185 near-surface wind vectors (\vec{u}_0 , 10 m winds ~~sampled from ERA5~~), which is denoted as
 186 DD_{topo} combined with DD . This component captures the influence of terrain on NH_3
 187 movement. For example, variations in elevation can create localized gradients that
 188 resemble NH_3 fluxes. The DD_{chem} estimator third term ~~considers~~ reflects the
 189 chemistry term ($k\Omega$), representing chemical interactions between NH_3 and atmospheric
 190 acids ~~which~~, resulting in the formation of particulate matter, ~~and is referred to as~~
 191 DD_{chem} along with the other terms. The full derivation of Eq. (1) is detailed in Sun
 192 (2022) and further explained by Ayazpour et al. (2024).

$$\begin{aligned}
 \langle E \rangle = & \underbrace{\langle \vec{u} \cdot (\nabla \Omega) \rangle}_{DD} + \underbrace{X \langle \Omega \vec{u}_0 \cdot (\nabla z_0) \rangle}_{DD_{topo}} + k \langle \Omega \rangle_{DD_{chem}} \quad (1)
 \end{aligned}$$

196 Here X and k represent the inverse scale height and inverse chemical lifetime,
 197 in which scale height represents the characteristic height of the species' vertical
 198 distribution, and chemical lifetime represents the average time before the species
 199 being removed by chemical reactions. $\langle \rangle$ denotes the spatiotemporal averaging
 200 operator already implemented in the physical oversampling framework (Sun et al.,
 201 2018). This method leverages the spatial variability of individual orbits and the data
 202 record to reduce noise and smooth spatial gradients in the gridded product. We
 203 employed the oversampling approach to aggregate Level 2 satellite data into a gridded
 204 Level 3 product at a 0.1° resolution on a daily scale. Data from IASI and CrIS were
 205 treated separately, but when multiple IASI and CrIS instruments were available on the
 206 same day, their data were merged together. Each Level 2 pixel was inflated spatially
 207 by a factor of 2 along both the major and minor axes of the ellipses, effectively filling

208 observational gaps and reducing noise. This is a critical step to enable spatial gradient
209 calculation when data coverage is sparse (e.g., only a single overpass is available).
210 This also limits the spatial resolving power to about twice the pixel size. ~~By smoothing~~
211 ~~spatial gradients, this method enables the generation of a more continuous and~~
212 ~~representative Level 3 NH₃ product, while acknowledging potential impacts on~~
213 ~~localized features.~~

214 X and k represent the inverse scale height and chemical reactivity, in which
215 scale height represents the characteristic height of the species' vertical distribution,
216 and chemical reactivity represents the inverse of average time before the species
217 being removed by chemical reactions. To improve the performance of the flux
218 estimates, we treat the X and k as fundamentally empirical fitting parameters within a
219 data-driven approach to ensure the resultant emission estimator centers around zero
220 where emissions are negligible. Although in theory X and k are tied to physically
221 meaningful quantities, their main purpose is to enhance emission estimators in the
222 presence of topography and chemistry using information contained by satellite
223 observations. As such, the quality of fitted X and k is subject to the quality and quantity
224 of available satellite data. Because of the gaps in individual IASI and CrIS pixels that
225 lead to undersampling of topography, we expect that X cannot fully account for
226 topography effects over complex terrains, an inherent limitation for scanning Fourier
227 Transform Spectrometers like IASI and CrIS.

228 To

229 ~~estimate gas flux, the inverse scale height (X) and inverse chemical lifetime (k)~~
230 ~~were determined using a linear regression approach. At location \mathbf{r} in regions where the~~
231 ~~emissions term (E) was are negligible compared to other terms ($E < 1 \times 10^{-9} \text{ mol m}^{-2}$,~~
232 ~~s^{-1} , based on bottom-up inventory from HEMCO; see Fig. S1 for spatial distribution),~~
233 ~~Eq. (1) can be reformulated into a multilinear regression form model by omitting the~~
234 ~~emission term:~~

$$235 \quad \langle \vec{u} \cdot (\nabla \Omega) \rangle = \beta_0 + \beta_1 \langle \Omega \vec{u}_0 \cdot (\nabla \mathbf{z}_0) \rangle + \beta_2 \langle \Omega \rangle + \varepsilon \quad (2)$$

236 Here β_1 ~~is an estimate of~~ corresponds to the negative inverse scale height ($-X$),
237 and β_2 is an estimate of ~~represents the negative inverse chemical lifetime ($-k$).~~ The
238 β_0 and ε account for the offset and random error, ~~respectively,~~ in the **DD estimator**
239 ~~term~~ $\langle \vec{u} \cdot (\nabla \Omega) \rangle$.

240 We conducted a two-step fitting process to estimate X and k NH₃ fluxes over
241 the CONUS following (Lonsdale and Sun, (2023)). The two fitting processes exclude
242 open water bodies and very rough terrains. The first fitting step focused on β_1 since
243 the fitting results for β_2 are usually noisy. The first-round ~~is~~ fitting for β_1 was limited in
244 moderately rough terrains with $0.001 \text{ m s}^{-1} < \langle \vec{u}_0 \cdot (\nabla \mathbf{z}_0) \rangle < 0.1 \text{ m s}^{-1}$. Once β_1 was
245 determined and then fixed, ~~and the second step focused on β_2 .~~ The second-round
246 fitting for β_2 is step was conducted in flat terrains ($\langle \vec{u}_0 \cdot (\nabla \mathbf{z}_0) \rangle < 0.001 \text{ m s}^{-1}$) with
247 moderate NH₃ VCD ~~column amounts~~ ($\Omega > 2.5 \times 10^{-5} \text{ mol m}^{-2}$) and minimal NH₃
248 emissions ($E < 1 \times 10^{-9} \text{ mol m}^{-2} \text{ s}^{-1}$) to isolate chemical transformation. To address the

249 challenges associated with a low signal-to-noise ratio, the fitting was performed over
 250 extended time intervals. Daily flux components, including $\langle \vec{u} \cdot (\nabla \Omega) \rangle$, $\langle \Omega \vec{u}_0 \cdot (\nabla \mathbf{z}_0) \rangle$
 251 and $\langle \Omega \rangle$, were first calculated at a spatial resolution of 0.1° . These values were then
 252 aggregated into six-month intervals ~~to improve signal-to-noise for IASI and four-~~
 253 ~~month intervals for CrIS, striking a balance between temporal resolution and noise~~
 254 ~~reduction.~~

255 We tested different spatial groupings, temporal averaging windows, and stricter
 256 maximum emission thresholds to refine the fitted X and k . For X , fitting the entire
 257 domain as a single group produces consistently positive and stable values, whereas
 258 subdividing the domain often introduces excessive noise (Fig. S2). Similarly, varying
 259 the temporal aggregation affects the stability of the fits (Fig. S3): shorter intervals
 260 produce noisier estimates, while longer intervals yield more robust results. We adopted
 261 a six-month aggregation interval as it provides reliable estimates across the entire
 262 period while retaining seasonal variability. The same settings were applied to k for
 263 consistency, though its performance is largely unaffected by these changes (Figs. S4-
 264 S5). Stricter emission thresholds for the chemistry term also have little impact (Fig. S6).

265 2.2.2 Uncertainty in DD analysis estimator

266 To estimate the uncertainty in DD estimator, we calculated DD ~~directional~~
 267 derivatives in both the zonal/meridional directions (\vec{x}/\vec{y}) and the diagonal directions
 268 (\vec{r}/\vec{s}). The final DD value was determined as the mean of the directional derivatives
 269 calculated along the \vec{x}/\vec{y} and \vec{r}/\vec{s} directions:

$$270 \quad DD = \text{mean}(DD_{\vec{x}/\vec{y}}, DD_{\vec{r}/\vec{s}}) \quad (3)$$

$$271 \quad DD_{\vec{x}/\vec{y}} = \vec{u} \cdot (\nabla \Omega)_{\vec{x}/\vec{y}} = \mathbf{u}_x \frac{\partial \Omega}{\partial x} + \mathbf{u}_y \frac{\partial \Omega}{\partial y} \quad (4)$$

$$272 \quad DD_{\vec{r}/\vec{s}} = \vec{u} \cdot (\nabla \Omega)_{\vec{r}/\vec{s}} = \mathbf{u}_r \frac{\partial \Omega}{\partial r} + \mathbf{u}_s \frac{\partial \Omega}{\partial s} \quad (5)$$

273 The difference between $DD_{\vec{x}/\vec{y}}$ and $DD_{\vec{r}/\vec{s}}$ was used to estimate the random
 274 errors (σ) of DD:

$$275 \quad \sigma = [\text{std}(DD_{\vec{x}/\vec{y}} - DD_{\vec{r}/\vec{s}})]/2 \quad (6)$$

276 We evaluated NH_3 fluxes at multiple spatial resolutions, including 0.2° , 0.1° , and
 277 0.04° . Consistent spatiotemporal patterns ~~are~~ observed across all grid scales (Fig.
 278 S72). A resolution of 0.1° ~~was~~ selected as the optimal balance, ensuring sufficient
 279 data coverage while effectively capturing spatial gradients in NH_3 fluxes (Wang et al.,
 280 2023).

281 2.3 Spatiotemporal pattern analysis

282 To analyze the spatial patterns of NH_3 fluxes, we focused on the period from
 283 September 2019 to April 2021. This timeframe was selected because both IASI and
 284 CrIS observations of NH_3 VCDs provided the most extensive data coverage, enabling
 285 a more reliable comparison between the two datasets. We also compared the spatial
 286 patterns of satellite-based NH_3 fluxes with bottom-up inventory NH_3 emissions and

287 land cover types. This comparison allows us to evaluate the consistency of satellite-
288 derived flux estimates with known NH₃ sources and their relationship to land use and
289 vegetation cover.

290 For the temporal pattern analysis, we utilized the full observational periods of
291 the datasets: January 2008 to December 2022 for IASI and June 2012 to December
292 2022 for CrIS. This extended temporal coverage allows for a comprehensive
293 understanding of NH₃ flux trends over time. To analyze the temporal patterns of NH₃
294 emission/deposition rates across high-flux regions, we calculated regional
295 emission/deposition rates by spatially integrating the fluxes within the source/sink
296 areas of each region. We examined the seasonal patterns of NH₃ emission/deposition
297 rates in both source and sink areas. These areas were defined based on the
298 uncertainty in *DD_estimator* quantified in Eq. 6. We classified locations where both
299 IASI- and CrIS-derived NH₃ fluxes exceeded 2σ as source regions and locations with
300 both fluxes lower than -2σ as sink regions. Additionally, we investigated the seasonal
301 variations in NH₃ emission/deposition rates derived from IASI and CrIS observations.
302 These were compared with seasonal signals in inventory data to evaluate the
303 consistency between top-down and bottom-up approaches.

304 3. Results

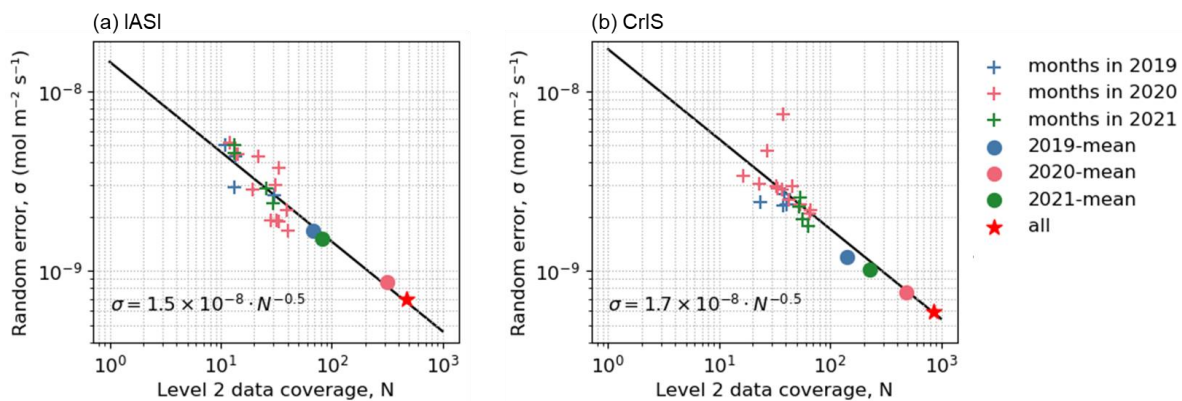
305 3.1 NH₃ flux estimation

306 In this study, we used the *DD_chemtopo-DD_chem_estimator* term as our
307 estimate for NH₃ flux estimates, and the chemical loss term ($k(\Omega)$) was excluded due
308 to its negligible contribution and poor fitting performance. Specifically, the derived k
309 values and its fitting R^2 were consistently near zero, indicating minimal contribution of
310 chemical loss for the overall fluxes (Fig. S3). In contrast, the wind-topography term
311 $(\Omega \vec{u}_0 \cdot (\nabla z_0))$ proved essential for addressing topographic biases in mountainous
312 regions (Fig. S8a, S8b4). Estimated NH₃ scale heights generally ranged from 1 to 2
313 km (Fig. S95), approximating the planetary boundary layer height. Higher scale heights
314 were observed when only one IASI instrument was operational as well as during
315 winter months in CrIS data, possibly due to weak thermal contrast. The chemistry term
316 contributes strongly in regions with high NH₃ column densities (Fig. S8c, S8d),
317 although the fitted chemical reactivities are generally weak (Fig. S9).

318 Fig. 1 shows the random errors, estimated through Eq. 6, in IASI- (a) and CrIS-
319 based (b) fluxes ~~over the CONUS from 2019 to 2021~~. These random errors were
320 calculated separately over monthly, annual, and total aggregated flux fields and plotted
321 against the mean coverage of Level 2 pixels used in the aggregation. These mean
322 coverage values were denoted by N and roughly correspond to the number of satellite
323 overpasses. Both IASI and CrIS observations demonstrated improved precision (lower
324 random errors) with increasing data coverage. The black lines in Fig. 1 represent the
325 theoretical scaling relationship, $\sigma = \sigma_0 / \sqrt{N}$, where σ_0 is the scaling factor derived
326 from the random errors of the monthly values:

$$327 \quad \sigma_0 = \exp(\text{mean}(\log(\sigma_i)) + 0.5 \cdot \text{mean}(\log(N_i))) \quad (7)$$

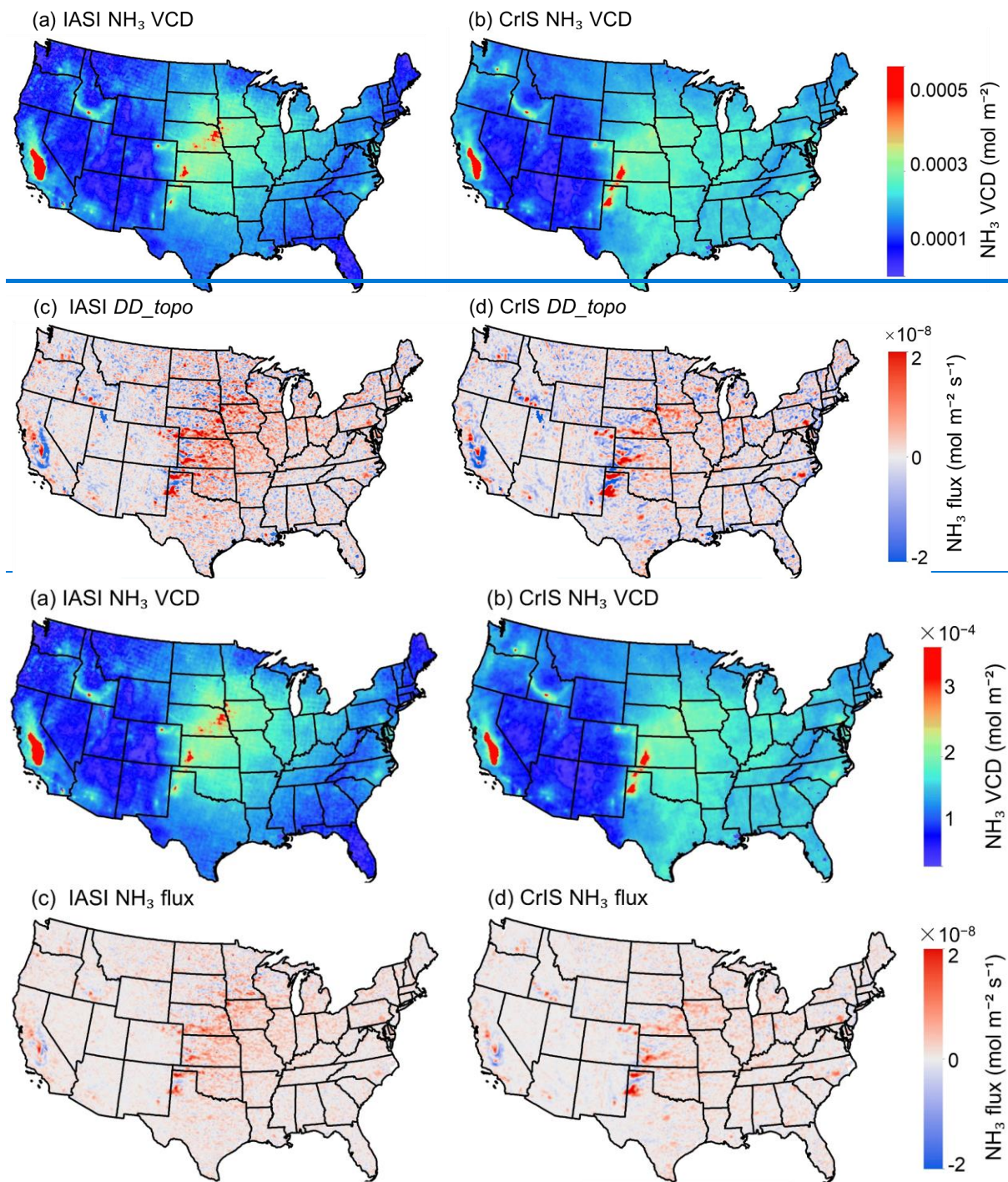
328 where σ_i and N_i represent the random errors and mean Level 2 data coverage for
 329 month i . If the random errors across different aggregation levels align with the $1/\sqrt{N}$
 330 scaling, it suggests that the random errors are independent and random. This
 331 alignment in Fig. 1 highlights the importance of extensive spatial and temporal
 332 coverage for reliable flux estimation. Additionally, the intercept of the black line with
 333 the vertical line at $N = 1$ provides the theoretical precision (σ_0) of flux estimated by a
 334 single, gap-free overpass of the satellite instrument. IASI showed slightly better
 335 single-overpass precision at 1.5×10^{-8} mol m² s⁻¹ for IASI, compared with 1.7×10^{-8} mol
 336 m² s⁻¹ for CrIS. However, the random errors are generally lower for CrIS when
 337 aggregated to the same intervals due to its denser Level 2 coverage than IASI.



338
 339 Figure 1. The relationship of random error (σ) and data coverage (N) for IASI (a) and
 340 CrIS (b) records [from Sep 2019 to Apr 2021](#). Dots represent random errors at various
 341 aggregation levels (monthly, annual, and total). The black lines represent the
 342 theoretical scaling relationship, $\sigma = \sigma_0 / \sqrt{N}$, where σ_0 denotes the single-overpass
 343 precision.

344 3.2 Spatiotemporal pattern of NH₃ flux over the CONUS

345 IASI and CrIS observations exhibited consistent hotspot regions in NH₃ VCDs
 346 and fluxes (Fig. 2). Spatially continuous hotspots included the San Joaquin Valley in
 347 California, the Snake River Valley in Idaho, the Texas panhandle and the Great Plains
 348 (Figs. 4-7), all regions known for intensive livestock production and high nitrogen
 349 fertilizer use (Liu et al., 2019). Discrete NH₃ emission hotspots also occurred in
 350 the eastern United States, notably in Southeastern Pennsylvania and Eastern North
 351 Carolina (Figs. 8, and 9), where concentrated animal feeding operations (CAFOs) are
 352 prevalent. Major NH₃ sinks ~~are were~~ located near sources, highlighting the localized
 353 deposition of NH₃ emissions. The primary sources of NH₃ emissions from satellite
 354 observations showed strong consistency with those from bottom-up inventories (Fig.
 355 S1), enhancing confidence in the reliability of satellite-based flux estimates for
 356 identifying key emission regions.



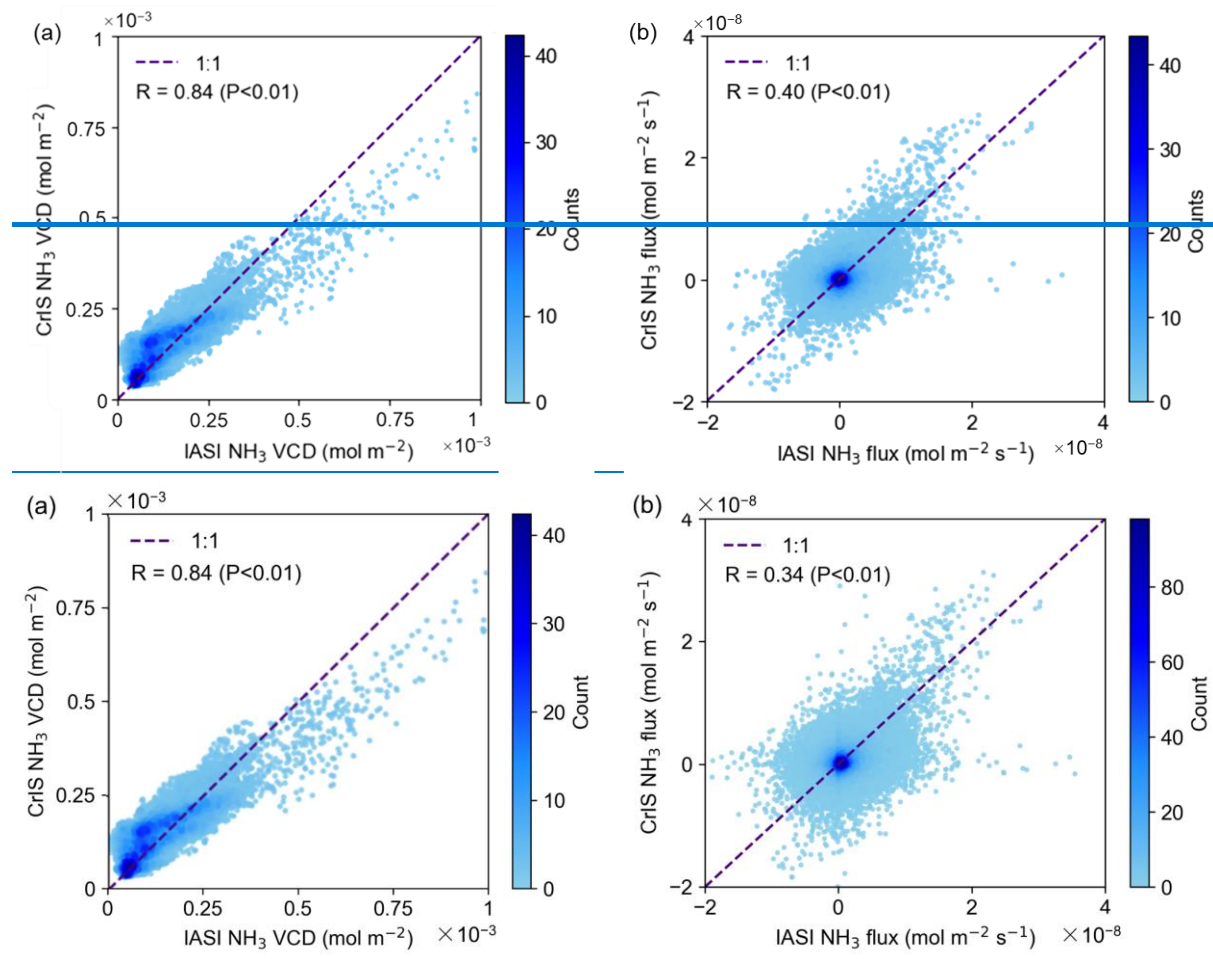
357

358

359 Figure 2. IASI- (a, c) and CrIS- (b, d) derived NH_3 VCD (a, b) and DD_{topo} -flux (c, d)
 360 averaged from Sep 2019 to Apr 2021 over the CONUS on a 0.1° grid.

361 Both NH_3 VCDs and flux estimates showed significant spatial agreement in IASI
 362 and CrIS, with correlation coefficients of $R = 0.84$ for VCDs and $R = 0.3440$ for NH_3
 363 fluxes ($P < 0.01$; Fig. 3). The VCD comparison reveals systematic differences between
 364 IASI and CrIS as different slopes and offsets in different regions (Fig. 3a). These
 365 offsets and proportional biases can propagate into flux calculations, where they
 366 manifest as amplified variability and reduced correlation (Fig. 3b). Frequently there

367 was an offset between VCDs from CrIS and IASI, manifested as consistent shifts or
 368 proportional scaling differences (Fig. 3a), impacting flux estimates in different ways.
 369 By concentrating on spatial gradients of VCDs, the directional derivative approach
 370 minimizes the impact of these offsets and results in comparable NH₃ flux patterns
 371 across both datasets. The lower correlation in for fluxes estimates compared to VCDs
 372 likely reflects compounded noises from derivative-based additional noise introduced
 373 during flux estimation, which relies on external datasets, assumptions, and signal
 374 differentiation.



377 Figure 3. Comparison of IASI- and CrIS-derived NH₃ VCD (a) and flux (b) averaged
 378 from Sep 2019 to Apr 2021.

379 The NH₃ fluxes over the CONUS exhibited a clear seasonal pattern, with higher fluxes
 380 observed in spring and summer and lower fluxes during winter (Fig. S156). CrIS-
 381 derived NH₃ flux showed strong signals throughout both spring and summer,
 382 reflecting consistent emissions during these warmer months. IASI-derived NH₃ flux
 383 displayed a more pronounced peak during summer. This difference may be attributed
 384 to the instruments' distinct observational characteristics, such as overpass times, and
 385 sensitivities under varying seasonal conditions, and differing detection limits. These
 386 spatiotemporal patterns are studied more closely in high-flux regions in the following
 387 section.

3.3 Spatiotemporal pattern of NH₃ flux in high-flux regions

Figs. 4-9 compare IASI- and CrIS-derived NH₃ fluxes with VCDs and bottom-up inventories across six major high-flux regions. Application of the flux estimator substantially sharpens spatial structures relative to VCDs. For instance, in the Snake River Valley (Fig. 5), enhanced VCDs appear as a broad belt, while the corresponding fluxes resolve into alternating hot and cold spots, indicating localized source–sink variability. Similar sharpening is evident in other regions, demonstrating the added value of the estimator in attributing fluxes to specific land cover types.

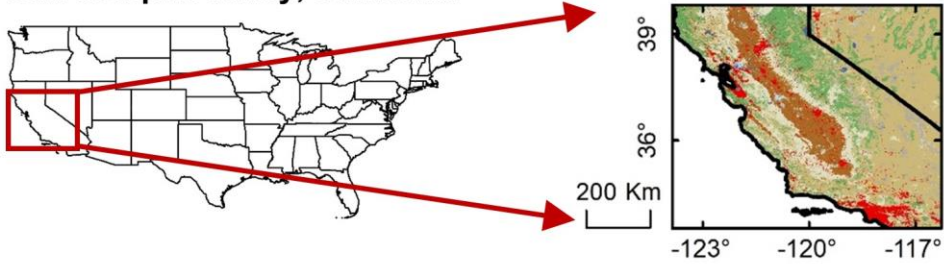
The two instruments yield broadly consistent spatial patterns of NH₃ source and sink, although systematic differences are observed. IASI-derived fluxes tend to resolve finer spatial detail, consistent with its smaller footprint and denser sampling, whereas CrIS-derived fluxes appear smoother but less noisy. These characteristics are complementary and together provide robust evidence for the spatial distribution of NH₃ fluxes.

Agricultural lands dominate as NH₃ source regions in all cases, with strong fluxes coinciding with intensive cropping and livestock production (e.g., San Joaquin Valley, Texas Panhandle, Great Plains). In contrast, natural and semi-natural landscapes function primarily as sinks. Vegetated landscapes—including forests, shrublands, and grasslands (Figs. 4-8), as well as wetlands (Fig. 9)—show consistent negative fluxes, likely reflecting deposition processes in proximity to nearby sources.

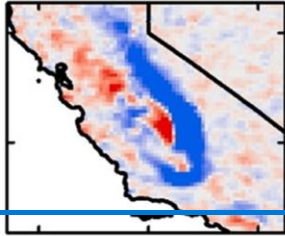
~~Both IASI and CrIS revealed consistent spatial patterns of NH₃ sources and sinks across key high-flux regions (Fig. 4-9), closely linked to underlying land cover types. Agricultural lands emerged as dominant NH₃ sources, while vegetated landscapes, including forests, shrublands, and grasslands (Fig. 4-8), as well as wetlands (Fig. 9), predominantly served as NH₃ sinks. These natural and managed ecosystems likely capture NH₃ through deposition processes near emission sources.~~

~~In areas with complex terrain, such as the mountainous regions near California's San Joaquin Valley, topographical artifacts were reduced when using *DD_topo* instead of *DD* (Figure 4 b, c, e, f), while *DD_topo* and *DD* exhibited similar flux values in flatter regions (Figure 5-9 b, c, e, f). Moreover, spatial patterns observed by IASI and CrIS closely align with bottom-up emission inventories, with correlation coefficients ranging from 0.038 to 0.786 over the key high-flux regions (Fig. S107), supporting the utility of satellite-derived flux estimates in characterizing NH₃ flux dynamics. Satellite-derived fluxes also align well with bottom-up inventories, with regional correlation coefficients ranging from 0.08 to 0.86 (Fig. S10). Agreement is highest in areas with dense agricultural activity (e.g., San Joaquin Valley), whereas discrepancies in regions such as the Great Plains and Snake River Valley suggest that inventories may not capture the full subregional variability evident in satellite observations. These results highlight both the consistency of satellite-derived fluxes with existing inventories and their capability to provide additional spatial detail.~~

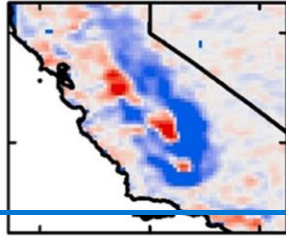
San Joaquin Valley, California



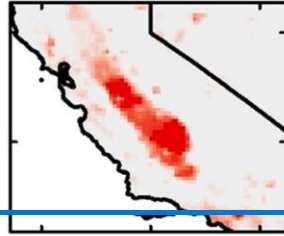
(b) IASI NH₃ flux: DD



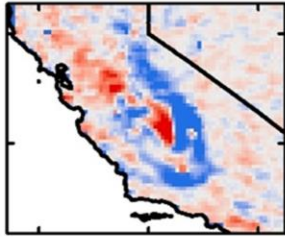
(c) CrIS NH₃ flux: DD



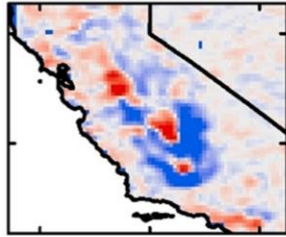
(d) Inventory emission



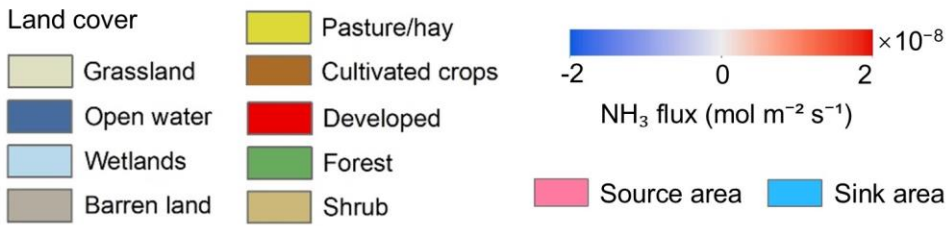
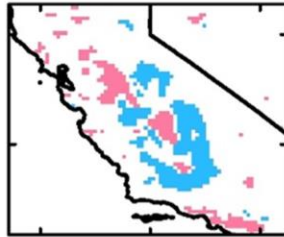
(e) IASI NH₃ flux: DD_topo

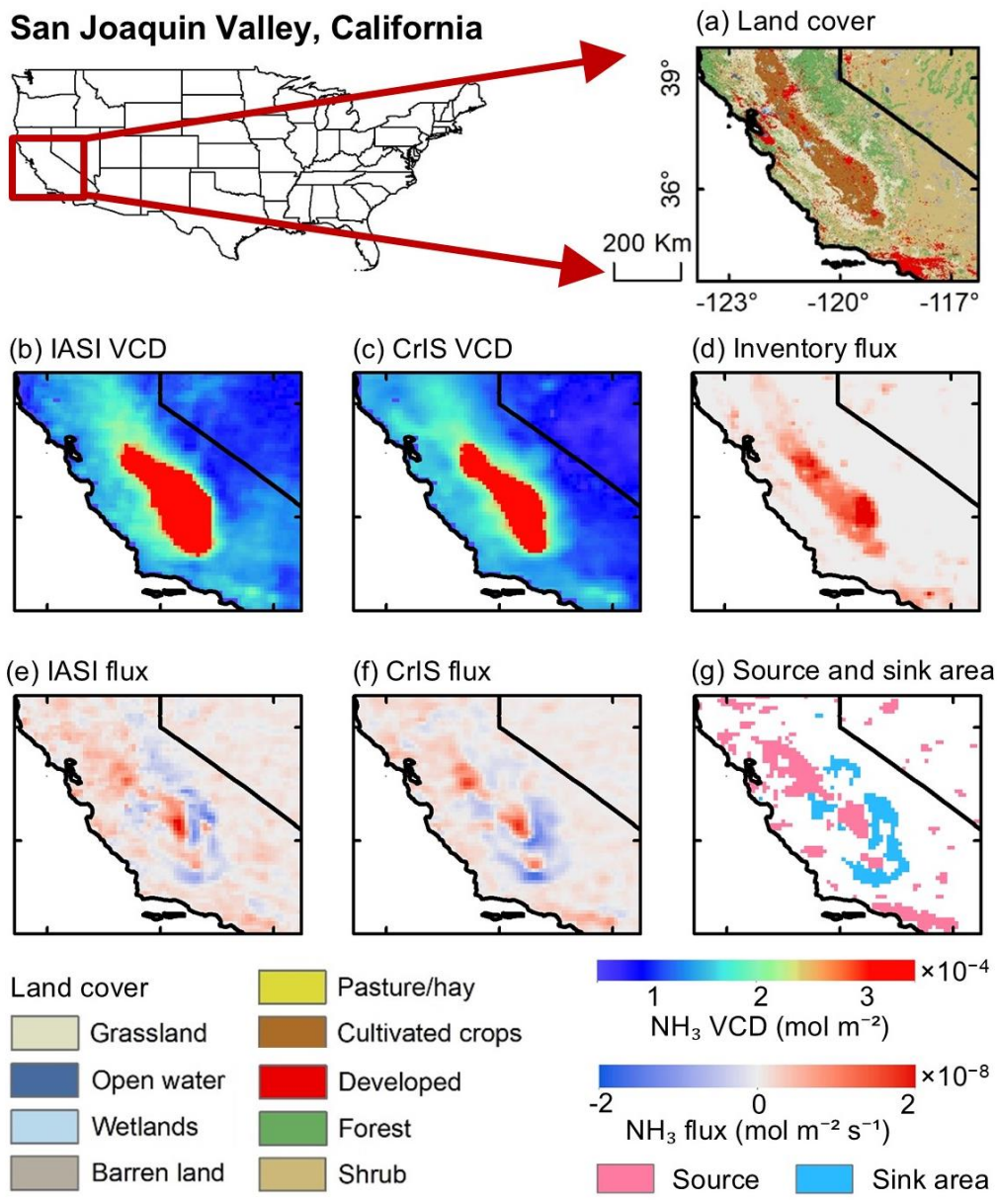


(f) CrIS NH₃ flux: DD_topo



(g) Source and sink area

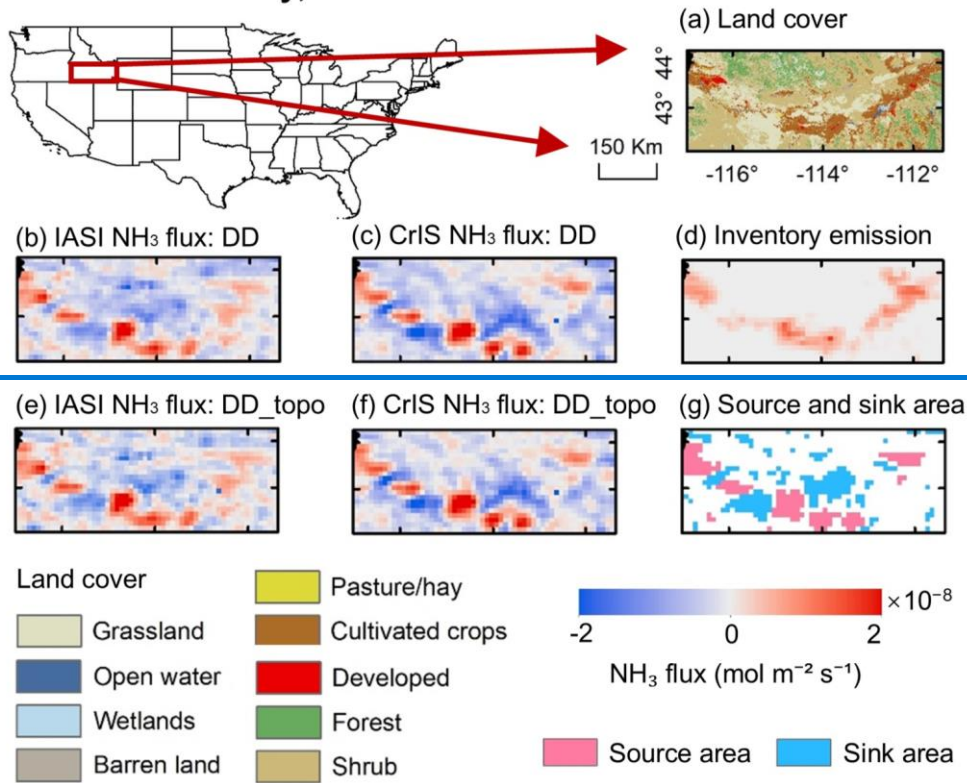




429

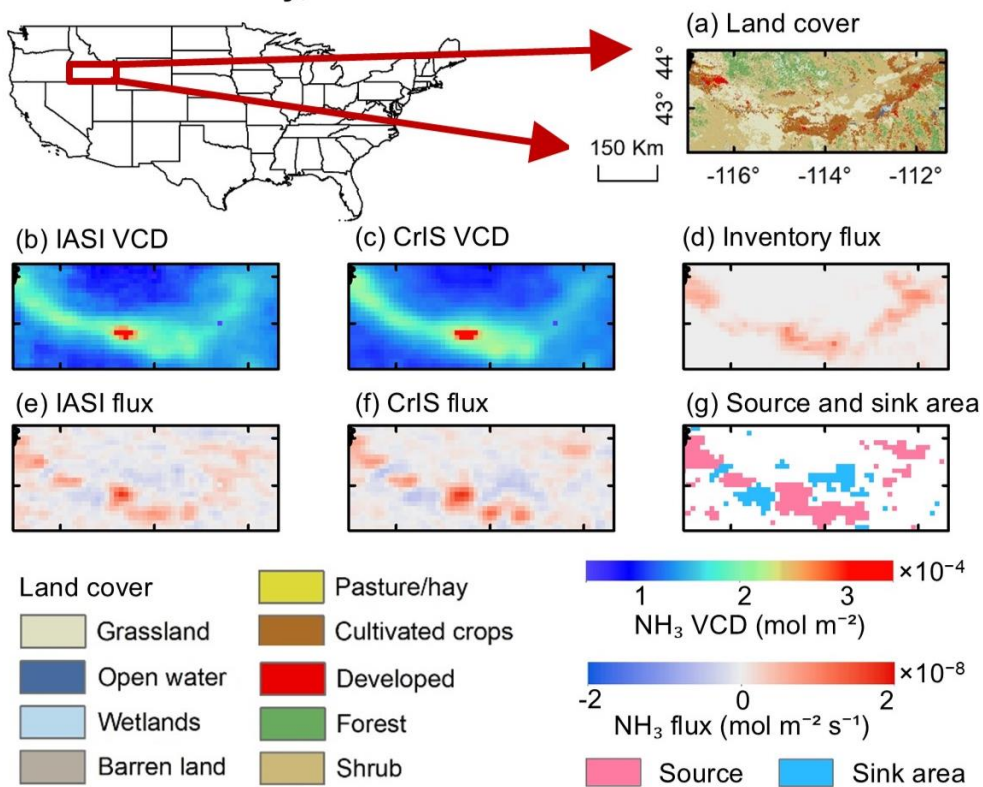
430 Figure 4. (a) Land cover types in the San Joaquin Valley in California. (b, c) VCD and
 431 (e, f) flux~~DD and (e, f) DD_topo flux~~ derived from IASI and CrIS NH₃ records. (d) NH₃
 432 emission from bottom-up inventory. (g) Source and sink areas of NH₃ flux, defined as
 433 the outside region of $\pm 2\sigma$ of **DD** from IASI and CrIS.

Snake River Valley, Idaho



434

Snake River Valley, Idaho



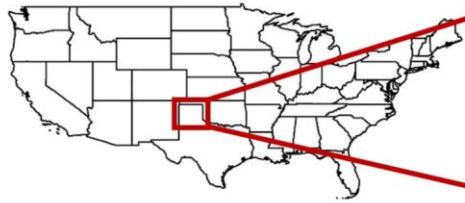
435

436 Figure 5. (a) Land cover types in the Snake River Valley in Idaho. (b, c) VCD and (e, f) flux_{DD} and (e, f) DD_topo flux derived from IASI and CrIS NH₃ records. (d) NH₃

437

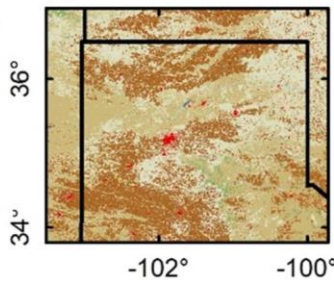
438 emission from bottom-up inventory. (g) Source and sink areas of NH₃ flux, defined as
439 the outside region of $\pm 2\sigma$ of **DD** from IASI and CrIS.

Texas panhandle

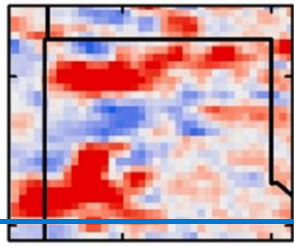


100 Km

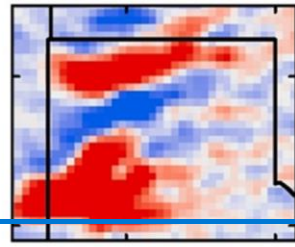
(a) Land cover



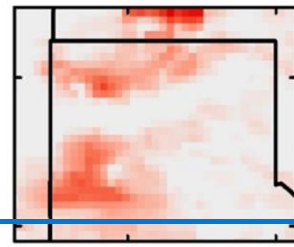
(b) IASI NH₃ flux: DD



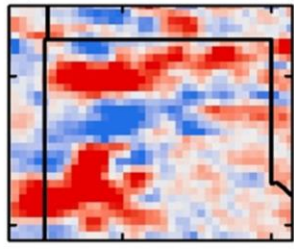
(c) CrIS NH₃ flux: DD



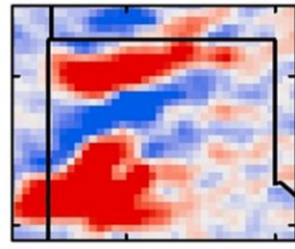
(d) Inventory emission



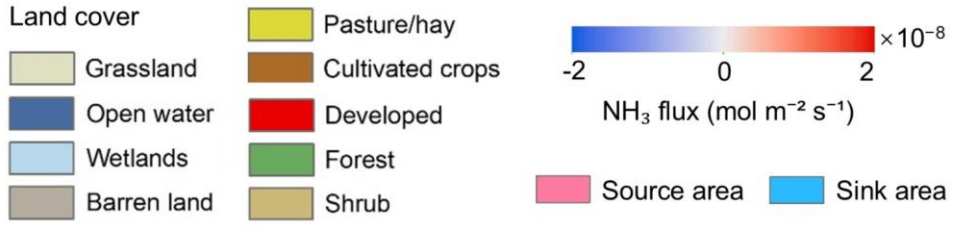
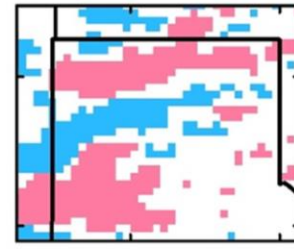
(e) IASI NH₃ flux: DD_topo

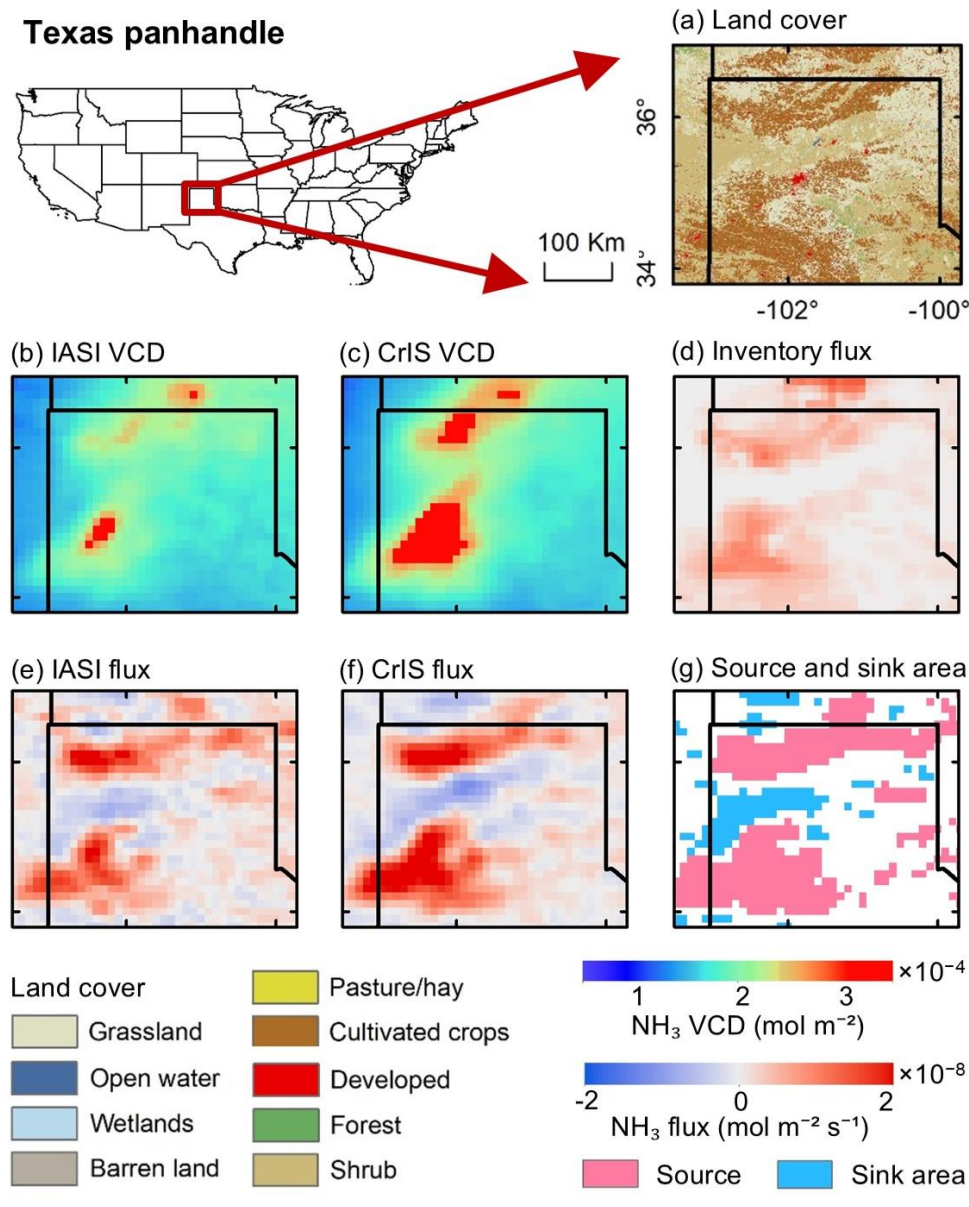


(f) CrIS NH₃ flux: DD_topo



(g) Source and sink area

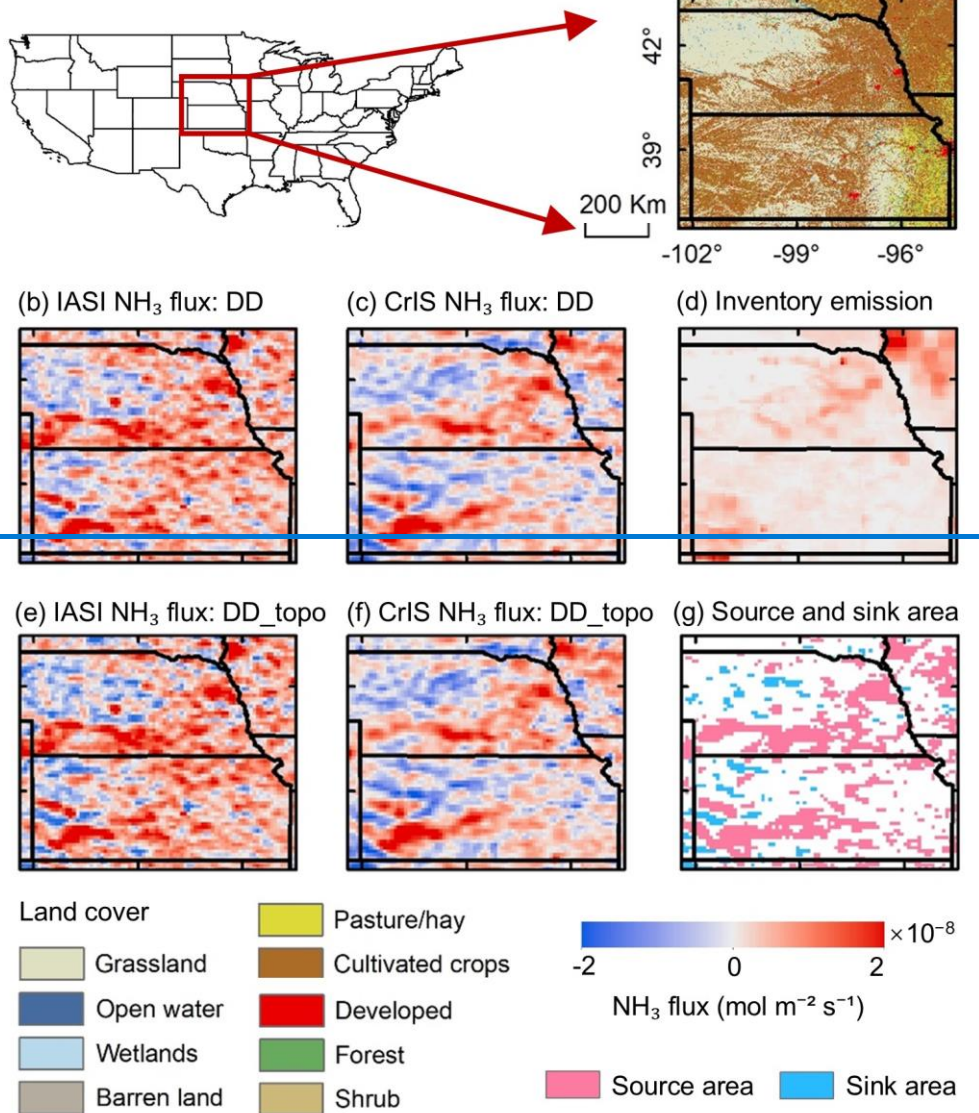


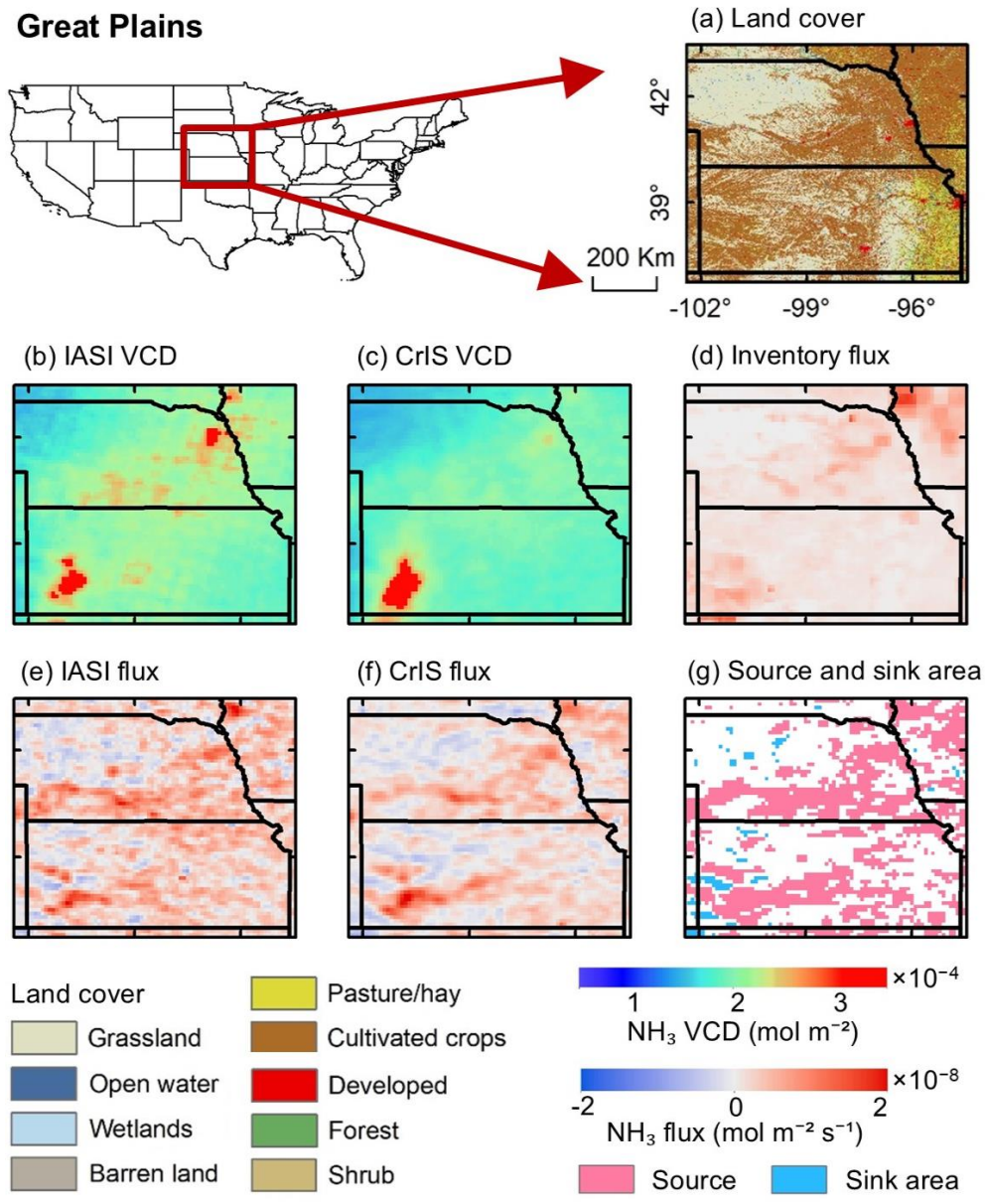


441

442 Figure 6. (a) Land cover types in the Texas panhandle. (b, c) VCD and (e, f) flux
 443 and and (e, f) *DD_topo* flux derived from IASI and CrIS NH₃ records. (d) NH₃ emission
 444 from bottom-up inventory. (g) Source and sink areas of NH₃ flux, defined as the outside
 445 region of $\pm 2\sigma$ of *DD* from IASI and CrIS.

Great Plains

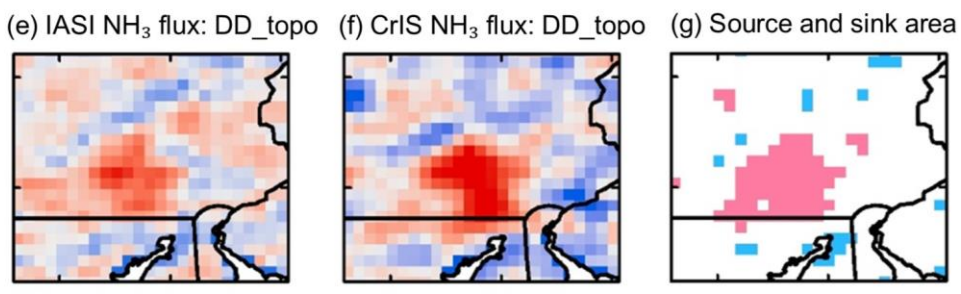
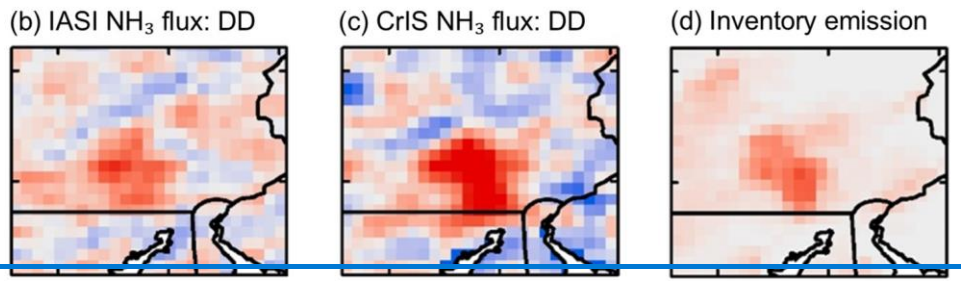
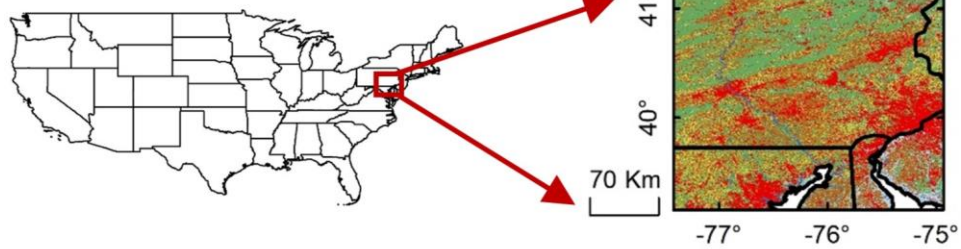




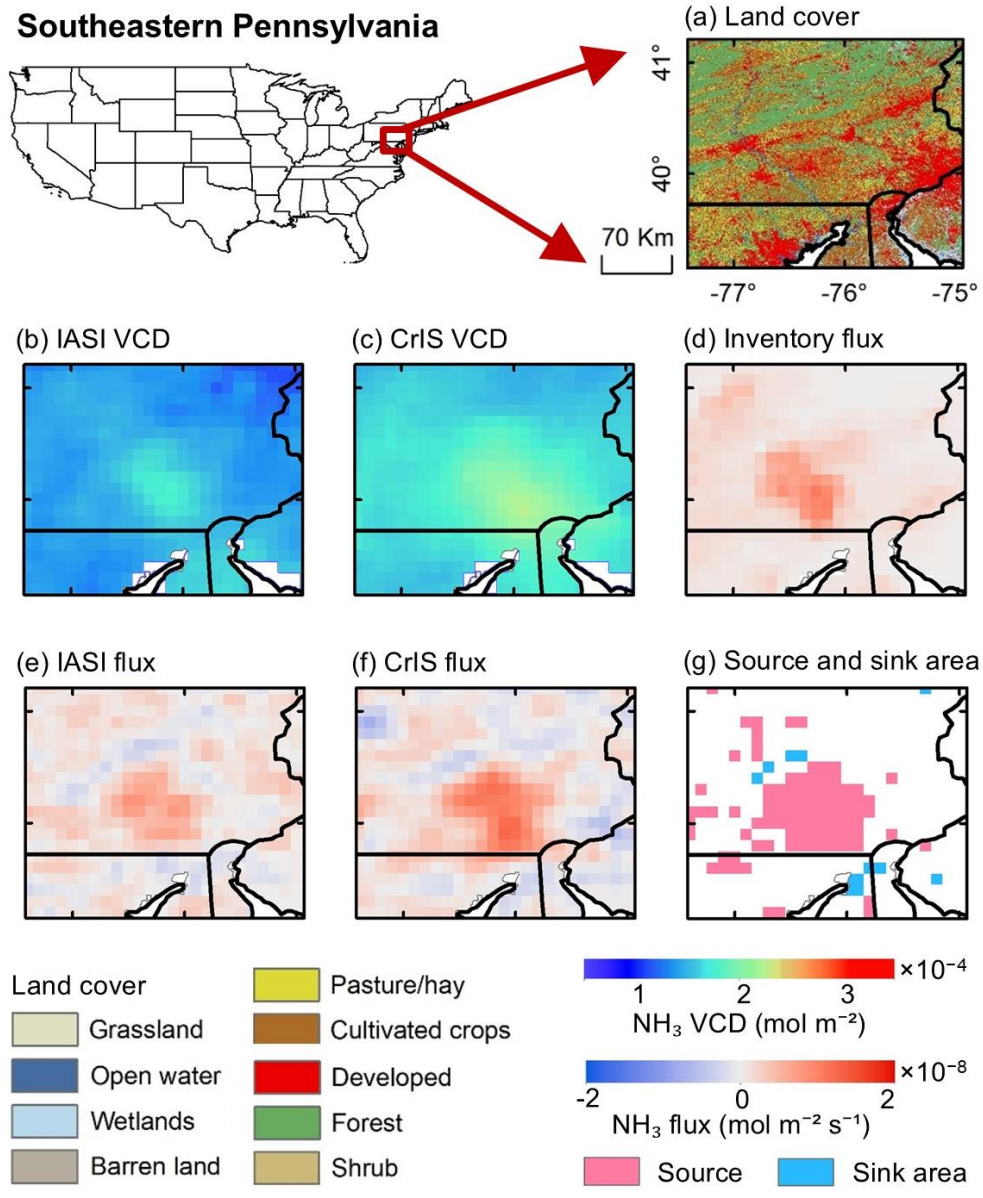
447

448 Figure 7. (a) Land cover types in the Great Plains. (b, c) VCD and (e, f) flux~~DD and~~
 449 and (e, f) DD_topo flux derived from IASI and CrIS NH₃ records. (d) NH₃ emission from
 450 bottom-up inventory. (g) Source and sink areas of NH₃ flux, defined as the outside
 451 region of $\pm 2\sigma$ of **DD** from IASI and CrIS.

Southeastern Pennsylvania



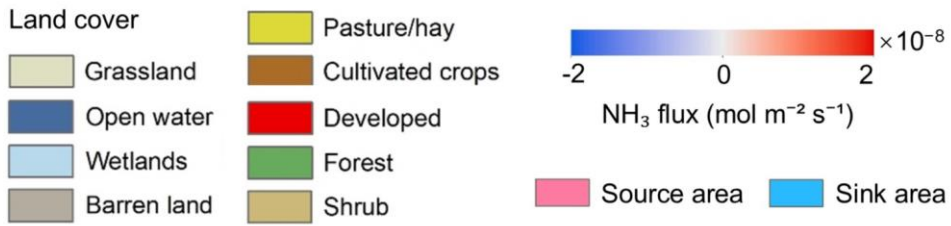
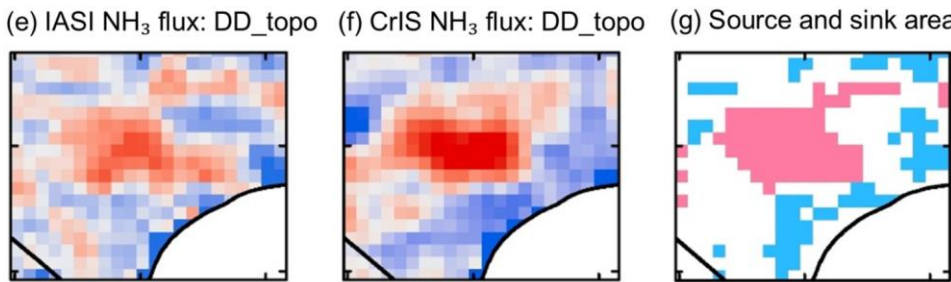
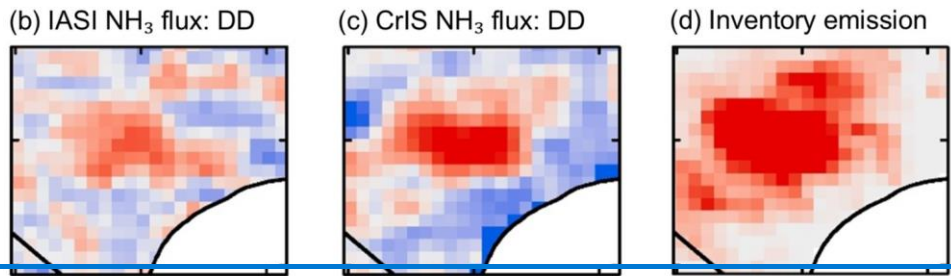
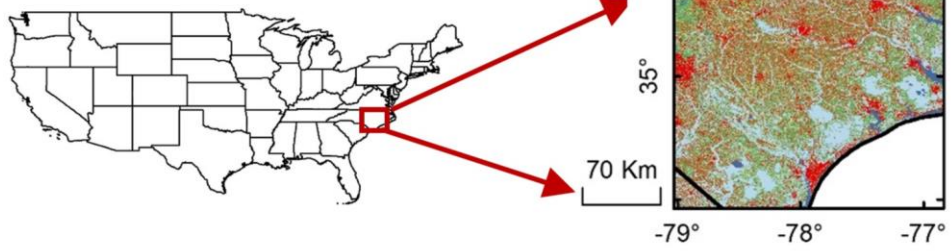
452

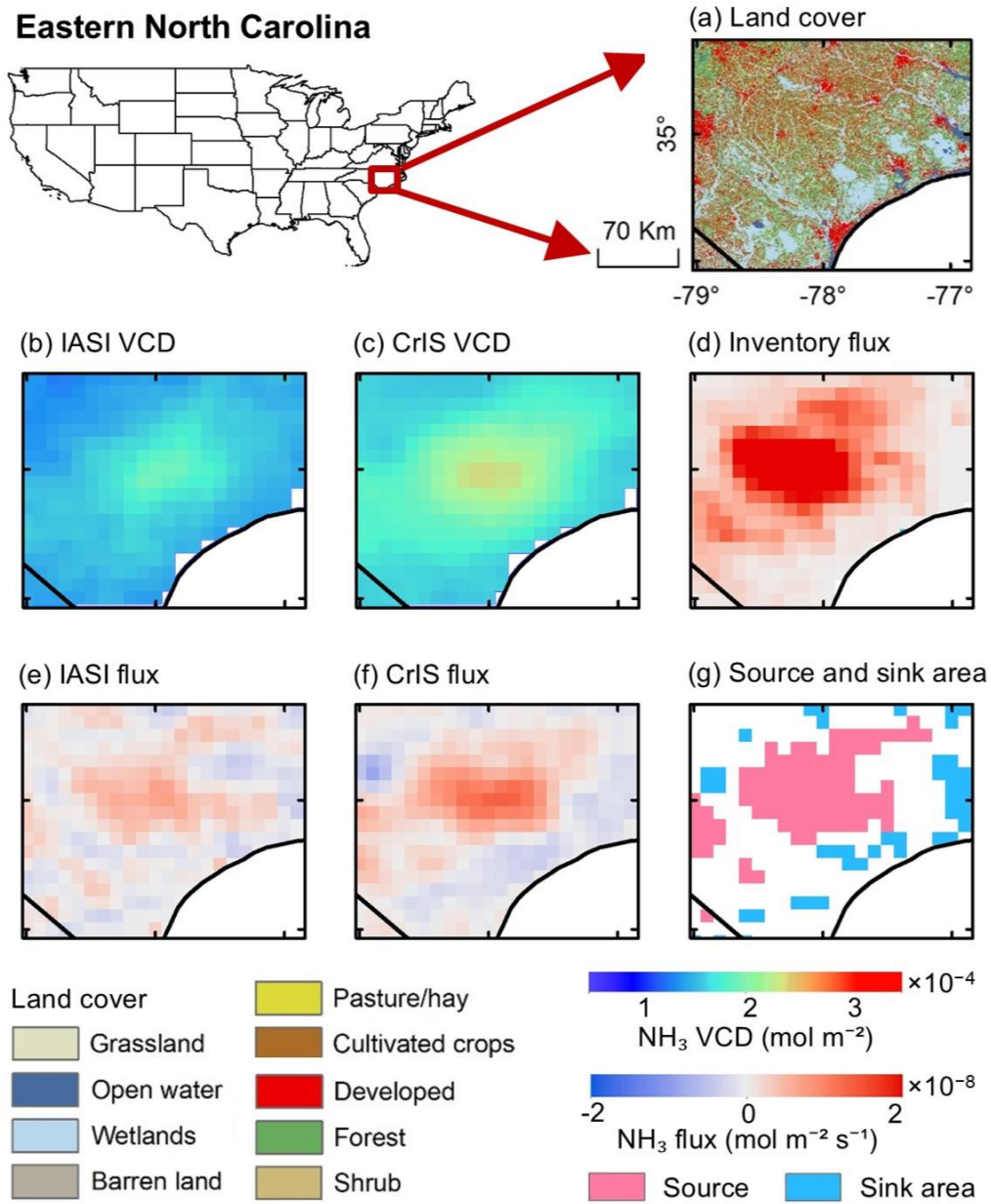


453

454 Figure 8. (a) Land cover types in Southeastern Pennsylvania. (b, c) VCD and (e, f)
 455 flux DD and and (e, f) DD_{topo} flux derived from IASI and CrIS NH₃ records. (d) NH₃
 456 emission from bottom-up inventory. (g) Source and sink areas of NH₃ flux, defined as
 457 the outside region of $\pm 2\sigma$ of DD from IASI and CrIS.

Eastern North Carolina





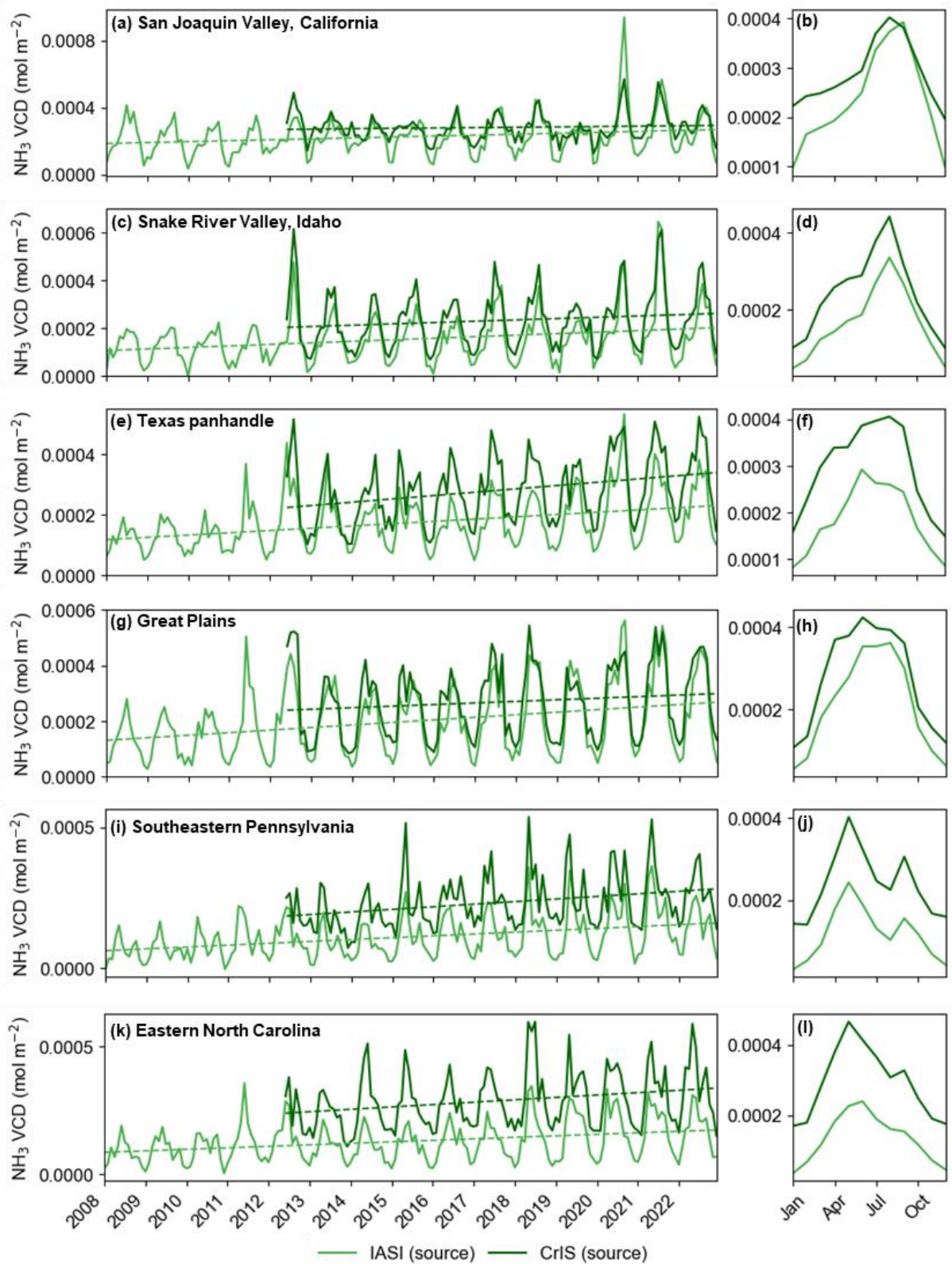
459

460 Figure 9. (a) Land cover types in Eastern North Carolina. (b, c) VCD and (e, f) flux
 461 and and (e, f) DD_{topo} flux derived from IASI and CrIS NH₃ records. (d) NH₃ emission
 462 from bottom-up inventory. (g) Source and sink areas of NH₃ flux, defined as the outside
 463 region of $\pm 2\sigma$ of DD from IASI and CrIS.

464 Figs. 10 and 11 illustrate the temporal and seasonal patterns of NH₃ VCDs and
 465 emission/deposition rates across major high-flux regions in the CONUS. Over time,
 466 these regions have exhibited upward trends in VCDs (Fig. 10), potentially indicating
 467 increasing NH₃ emissions. Seasonal cycles in NH₃ VCDs awere distinct across all
 468 regions, with higher values in the warm seasons and lower values in winter, driven by
 469 increased agricultural activities, such as livestock operations and fertilizer application,
 470 as well as enhanced volatilization during higher temperatures. Observations from CrIS
 471 (dark lines) and IASI (light lines) awere generally aligned, though CrIS often reportsed
 472 higher VCDs. Differences between CrIS and IASI awere largely consistent across

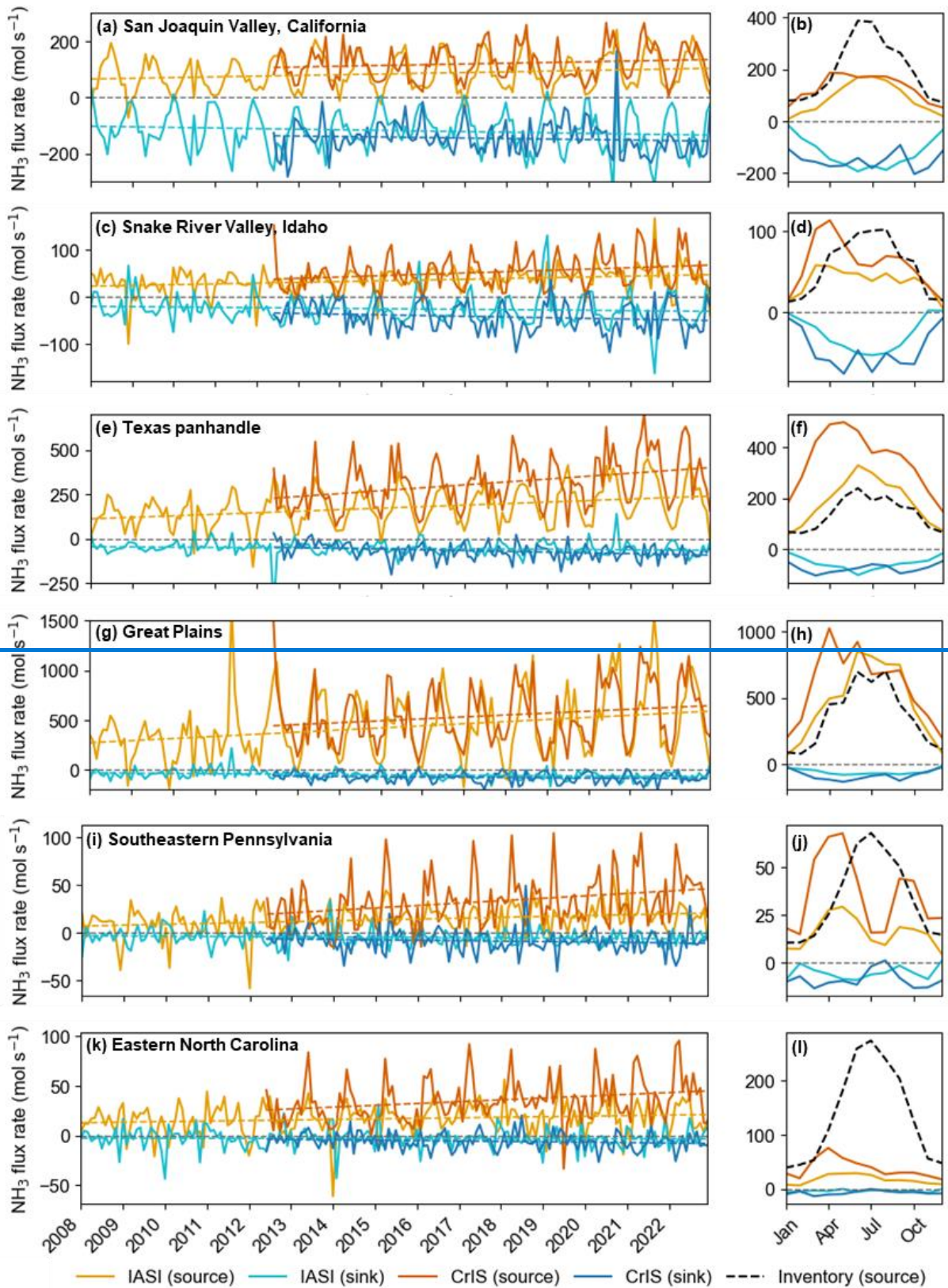
473 seasons, but tended to be more pronounced in the warm months in regions such as
474 the Texas Panhandle and Great Plains (Fig. 10 f, h).

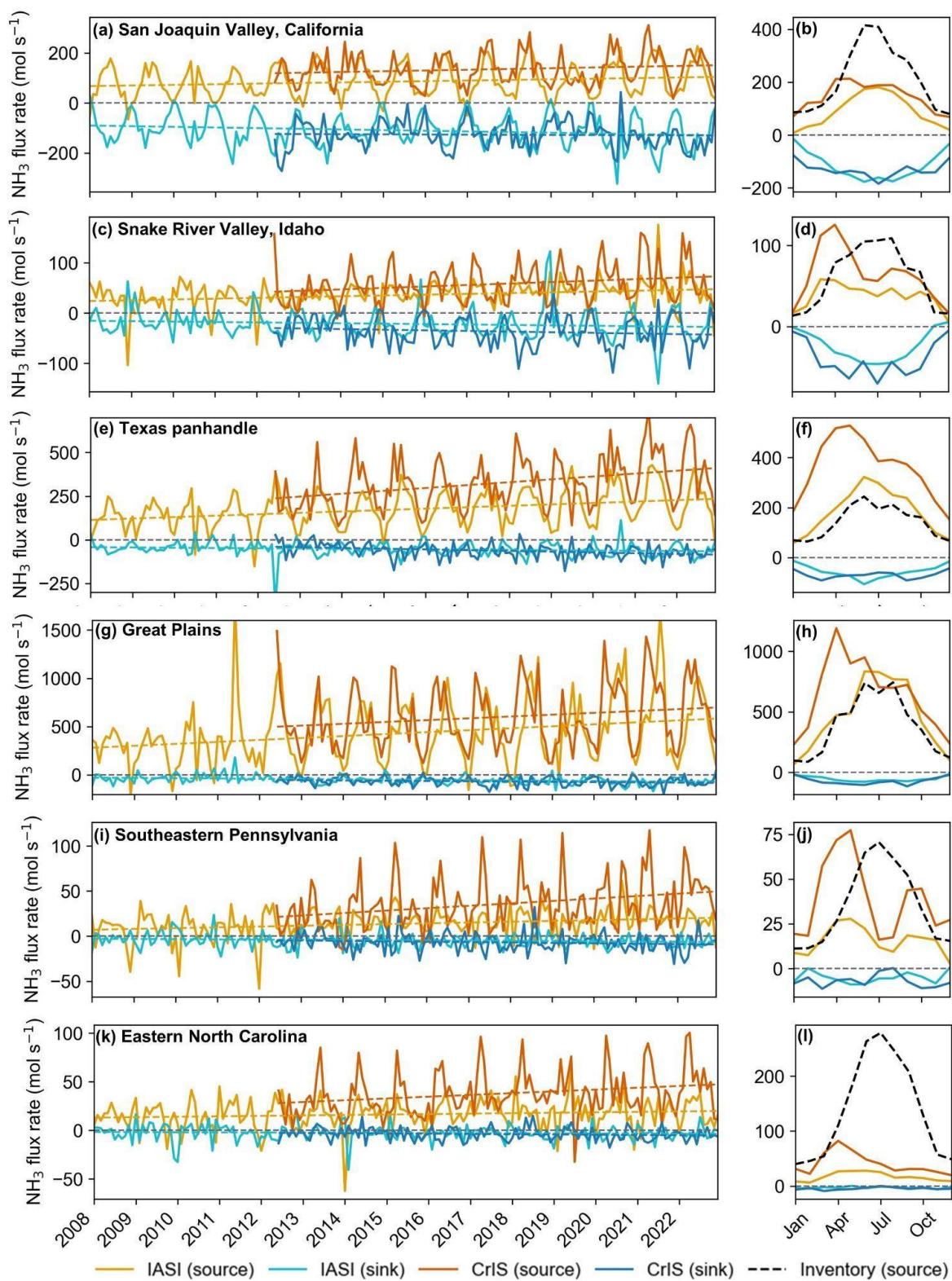
475 Satellite-derived NH₃ fluxes, including emissions (positive fluxes, yellow lines)
476 and depositions (negative fluxes, blue lines), have exhibited increasing trends over
477 time (Fig. 11). Seasonal patterns in NH₃ fluxes revealed mirrored those of VCDs, with
478 emissions peaking in warm months due to heightened agricultural activity and elevated
479 temperatures, while deposition rates also increased during this period, though with
480 smaller magnitudes. This synchronization between emissions and deposition rates
481 suggests that a significant proportion of emitted NH₃ was deposited locally. A
482 comparison with bottom-up inventory data revealed key differences. Satellite-based
483 estimates captured diurnal patterns, with IASI observing morning emissions (09:30
484 LST) and CrIS capturing midday emissions (13:30 LST), whereas inventory data
485 represent modeled averages. In regions like the Texas Panhandle and Great
486 Plains (Fig. 11 f, h), satellite observations showed higher seasonal emission peaks
487 than inventory models, indicating potential underestimation of seasonal emissions in
488 the inventories. Conversely, inventories overestimated emissions compared to
489 satellite observations in the San Joaquin Valley and Eastern North Carolina (Fig. 11 b,
490 l). Seasonality in inventory emissions is aware consistent with IASI observations in
491 some regions, such as the Texas Panhandle and Great Plains (Fig. 11 f, h). However,
492 in the Snake River Valley, Southeastern Pennsylvania, and Eastern North Carolina
493 (Fig. 11 d, j, l), inventory displayed entirely different seasonal signals compared to
494 satellite data, underscoring the value of satellite observations in capturing the temporal
495 dynamics of agricultural emissions. CrIS consistently observed larger NH₃ emissions
496 than IASI, while deposition differences were smaller. Notably, the difference in CrIS
497 and IASI was most obvious in spring across all the regions. CrIS detected early spring
498 peaks in regions such as like the Texas Panhandle and Great Plains (Fig. 11 f, h),
499 which were not captured by IASI, highlighting variations in sensitivity between the two
500 instruments.



501
 502 Figure 10. Temporal series (a, c, e, g, i, k) and seasonal pattern (b, d, f, h, j, l) of NH₃
 503 VCD at source areas from IASI (light lines) and CrIS (dark lines) records in the San
 504 Joaquin Valley in California (a, b), Snake River Valley in Idaho (c, d), Texas panhandle
 505 (e, f), Great Plains (g, h), Southeastern Pennsylvania (i, j), and Eastern North Carolina

506 (k, l). The dashed lines represent trends derived using linear regression applied to the
507 monthly temporal series data.





509

510 Figure 11. Temporal series (a, c, e, g, i, k) and seasonal pattern (b, d, f, h, j, l) of NH₃
 511 emission/deposition rate from IASI (light lines) and CrIS (dark lines) records, and NH₃
 512 emission rate at source areas from bottom-up inventory (black dashed lines) in the
 513 San Joaquin Valley in California (a, b), Snake River Valley in Idaho (c, d), Texas

514 panhandle (e, f), Great Plains (g, h), Southeastern Pennsylvania (i, j), and Eastern
515 North Carolina (k, l).

516 4. Discussion

517 4.1 Robustness of satellite-based NH₃ flux estimates

518 Our findings underscore the value of satellite observations in advancing the
519 characterization of NH₃ fluxes. With the ability to produce flux estimates at relatively
520 fine spatial and temporal scales, satellite datasets can help understand emission and
521 deposition dynamics, thereby providing additional insights into seasonal variability that
522 traditional bottom-up inventories often miss.

523 A key advancement of this work is the combined use of IASI (morning overpass)
524 and CrIS (midday overpass). By combining these two instruments, it is possible to
525 achieve quasi-diurnal coverage and capture the sub-daily variability of NH₃ fluxes that
526 is challenging to discern with a single satellite product. This synergy is especially
527 evident in spring, when the transition from cooler morning to warmer midday conditions
528 can amplify NH₃ emissions. CrIS frequently shows an early-spring emission pulse that
529 is less pronounced in IASI data, especially in areas with substantial emissions (Fig.
530 11). Spring emerged as a critical transitional period, characterized by moderate
531 temperature differences between IASI and CrIS observations (Fig. S118) and relatively
532 high NH₃ fluxes (Fig. 10). [This difference may be attributed to the instruments' distinct
533 observational characteristics, such as overpass times, and sensitivities under varying
534 seasonal conditions, and differing detection limits.](#) A further strength of combining
535 different instruments lies in the expanded data coverage. Our error analysis indicates
536 a strong $1/\sqrt{N}$ dependence of random errors (Fig. 1), suggesting that the flux
537 uncertainties drop significantly with denser observations (Wang et al., 2023). By
538 merging multiple overpasses and employing spatial smoothing through physical
539 oversampling, we can substantially reduce random errors and enhance flux
540 [reliabilityprecision.](#)

541 Our satellite-based approach demonstrates some advantages over bottom-up
542 inventories, in which satellite-based observations detect finer-scale fluxes and uncover
543 seasonal patterns not always well represented in inventory data. Previous studies have
544 shown that top-down approaches using satellite observations significantly reduce
545 uncertainties in emission estimates (Byrne et al., 2024; Evangeliou et al., 2021). Each
546 method has unique strengths, and integrating them offers a robust pathway to make
547 more reliable and comprehensive estimates (Tian et al., 2020). While bottom-up
548 methods provide critical context on local processes such as fertilizer application
549 (Zhang et al., 2018), satellite data can validate or refine emission factors and aid in
550 reconciling regional to continental-scale uncertainties (Chen et al., 2021; Zhu et al.,
551 2013).

552 Despite their advantages, infrared-based NH₃ satellite retrievals have certain
553 limitations. [WFor instance, weak thermal contrast and cooler temperaturesthermal
554 signal, especially common](#) in winter, reduces [the](#) detection efficiency [of the infrared](#)

sensors (Clarisse et al., 2010; Sutton et al., 2013), and retrievals are limited to daytime clear-sky conditions, potentially biasing results due to NH₃'s strong diurnal cycle (Blanes-Vidal et al., 2008). IASI columns differ from ground-based measurements by $-32 \pm 56\%$ (Dammers et al., 2016), with errors highly dependent on thermal contrast (Van Damme et al., 2014). CrIS retrievals show ~10–30% error in total columns and larger uncertainty at low concentrations (Shephard et al., 2020). While both IASI and CrIS have demonstrated good long-term stability through calibration monitoring and ground-based validation (Clarisse et al. 2023; Van Damme et al. 2015; Chen et al. 2014; Dammers et al. 2017), subtle time - dependent biases cannot be fully excluded. Overcoming these challenges requires ongoing refinements to retrieval algorithms, particularly in cloud screening and thermal contrast corrections. As satellite missions and retrieval techniques continue to improve, we anticipate further reductions in retrieval biases and increases in data coverage, leading to even more reliable, near real-time estimates of NH₃ fluxes.

4.2 Spatiotemporal pattern of NH₃ flux

Beyond demonstrating robust satellite-based flux estimates, our analysis exposes clear spatial gradients and pronounced seasonality in NH₃ sources and sinks across the CONUS. Both IASI- and CrIS-derived fluxes identify consistent emission hotspots (Fig. 2) in the San Joaquin Valley (California), Snake River Valley (Idaho), Texas Panhandle, Great Plains, Southeastern Pennsylvania, and Eastern North Carolina (Figs. 4-9), characterized by intensive livestock operations and fertilizer application, which are consistent with existing maps of VCD hotspots (Chen et al., 2021; Wang et al., 2021) and emission mapping efforts (Evangeliou et al., 2021; Zhang et al., 2012; Sitwell et al., 2022). Other than emissions, our directional derivariate approach can detect sinks in vegetation-dense areas surrounding these emission sources, such as shrublands and scrublands, forests, grasslands, and wetlands, highlighting the role of nearby ecosystems in capturing NH₃ through deposition (Pan et al., 2021; Hu et al., 2021; Azouz et al., 2019; Kharol et al., 2018; Loubet et al., 2009). Similar hotspots of deposition downwind of intensive agricultural regions have been reported in model-based studies (Ellis et al., 2013; Hu et al., 2021; Zhang et al., 2012). These hotspots often coincide with high NH₃ loadings, large leaf area indices, and micrometeorological conditions favorable for stomatal and cuticular uptake (Sutton et al., 2009). This localized deposition has caused negative effects (e.g., soil acidification, eutrophication, biodiversity loss) of excess nitrogen deposition in sensitive ecosystems (Krupa, 2003; Pearson and Stewart, 1993), and ~~our results indicate point to~~ an upward trend in deposition (Fig. 11) that could amplify these impacts in the future.

Our results further indicate that deposition near sources is the predominant NH₃ removal pathway, rather than chemical transformation. This pattern is likely reflecting acid-limited conditions that suppress the formation of ammonium particulate matter (Pan et al., 2024). The relatively high dry deposition velocity of NH₃ (Hesterberg et al., 1996; Kirchner et al., 2005) and its slow chemical reaction rate with acidic species under acid-limited conditions (Sutton et al., 2009) reinforce the small contribution of

597 chemical pathways to NH₃ removal in many agricultural hotspots. Consistent with
598 recent modeling and observational studies (Luo et al., 2022; Warner et al., 2017), our
599 multi-year analyses reveals a gradual but evident increase in NH₃ fluxes over time
600 (Fig. 11), raising concerns that expanding agricultural activities may be offsetting air
601 quality gains achieved through reductions in nitrogen oxides (Li et al., 2016).

602 The seasonality of NH₃ fluxes (Fig. 11) is closely linked to meteorological factors
603 and agricultural activities, with enhanced fluxes in warm months due to increased
604 volatilization from livestock production and fertilizer application (Tang et al., 2018;
605 Warner et al., 2017; Nelson et al., 2017) and relatively lower fluxes in winter. These
606 seasonal signals underscore the importance of timely policy by controlling agricultural
607 practices to manage NH₃ emissions and subsequent environmental impacts.
608 Successful examples from Western Europe demonstrate that targeted regulations can
609 effectively reduce NH₃ emissions (Liu et al., 2022). Furthermore, reducing ammonia
610 emissions proves more cost-effective than controlling nitrogen oxides for mitigating
611 PM_{2.5} pollution (Gu et al., 2021). These findings emphasize the profound influence of
612 agricultural practices and temperature regimes on NH₃ flux dynamics, underscoring
613 the need for integrated strategies to address both local and regional air quality
614 concerns.

615 5. Conclusion

616 This study highlights the utility of the directional derivative approach applied to
617 satellite data for estimating NH₃ fluxes across the CONUS. By leveraging IASI and
618 CrIS observations, we addressed challenges related to spatial variability,
619 topographical artifacts, and seasonal signals, providing insights into NH₃ emission and
620 deposition dynamics.

621 Our findings indicate that deposition serves as a significant removal pathway
622 for NH₃. NH₃ sinks were predominantly located near source regions, particularly in
623 vegetation-dense areas where rapid dry deposition occurs. Major NH₃ emission
624 hotspots were identified in agricultural regions, including the San Joaquin Valley in
625 California, the Snake River Valley in Idaho, the Texas Panhandle, the Great Plains,
626 Southeastern Pennsylvania, and Eastern North Carolina. NH₃ fluxes exhibited a clear
627 seasonal pattern, peaking during warm months due to increased volatilization from
628 agricultural activities and declining during winter with lower temperatures. Increasing
629 trends in NH₃ fluxes highlight the growing impact of intensified agricultural practices,
630 emphasizing the need for improved monitoring and mitigation strategies. While
631 satellite-derived NH₃ fluxes strongly aligned with bottom-up inventories, satellite
632 observations offered additional value by capturing diurnal variabilities.

633 This study demonstrates the value of satellite observations for high-resolution
634 monitoring of reactive nitrogen cycling, particularly in regions with limited ground-
635 based measurements. These findings offer critical insights for understanding nitrogen
636 loss and deposition processes, supporting enhanced nitrogen management strategies
637 and environmental policy efforts aimed at mitigating ammonia's environmental impacts
638 and managing reactive nitrogen in the atmosphere.

639 **Code and data availability**

640 The IASI L2 ammonia satellite observations are available from the AERIS data
641 infrastructure (<https://doi.org/10.25326/10>, Clarisse et al., 2018). The CrIS L2
642 ammonia satellite observations can be obtained by request to Mark Shephard
643 (mark.shephard@ec.gc.ca). The ERA5 data are available at
644 <https://doi.org/10.24381/cds.adbb2d47> (Hersbach et al., 2023). Code for flux
645 estimation can be found at https://github.com/Kang-Sun-CfA/Oversampling_matlab.
646 [The annual ammonia flux dataset derived in this study \(2008–2022 for IASI and 2012–](https://doi.org/10.6084/m9.figshare.30229648)
647 [2022 for CrIS, 0.1° resolution over the CONUS\) is publicly available at Figshare](https://doi.org/10.6084/m9.figshare.30229648)
648 [\(<https://doi.org/10.6084/m9.figshare.30229648>\).](https://doi.org/10.6084/m9.figshare.30229648)

649 **Author contribution**

650 KS and KG designed the study and coordinated the paper. LC, MVD and PFC
651 contributed to the IASI ammonia observations. KCP and MWS provided the CrIS
652 ammonia observations. KS wrote the code for the directional derivative approach. ZL
653 performed the estimations and analyses, and wrote the paper. All the authors
654 contributed to the final version of the paper.

655 **Competing interests**

656 The contact author has declared that neither of the authors has any competing
657 interests.

658 **Acknowledgments**

659 The authors acknowledge support from NASA's Interdisciplinary Science (IDS)
660 Program. KG and ZL acknowledge support from USDA NIFA and Hatch. KS
661 acknowledges support from NSF CAREER (AGS 2338758).

662 **References**

- 663 Adams, C., McLinden, C. A., Shephard, M. W., Dickson, N., Dammers, E., Chen, J., Makar,
664 P., Cady-Pereira, K. E., Tam, N., Kharol, S. K., Lamsal, L. N., and Krotkov, N. A.:
665 Satellite-derived emissions of carbon monoxide, ammonia, and nitrogen dioxide from
666 the 2016 Horse River wildfire in the Fort McMurray area, *Atmos. Chem. Phys.*, 19, 2577–
667 2599, <https://doi.org/10.5194/acp-19-2577-2019>, 2019.
- 668 Asman, W. A. H., Sutton, M. A., and Schjørring, J. K.: Ammonia: emission, atmospheric
669 transport and deposition, *New Phytologist*, 139, 27–48, <https://doi.org/10.1046/j.1469-8137.1998.00180.x>, 1998.
- 670
- 671 ~~[Ayazpour, Z., Sun, K., Zhang, R., and Shen, H.: Evaluation of the directional derivative](#)~~
672 ~~[approach for timely and accurate satellite-based emission estimation using chemical](#)~~
673 ~~[transport model simulation of nitrogen oxides, ESS Open Archive,](#)~~
674 ~~<https://doi.org/10.22541/essoar.173046708.85066876/v1>, 2024.~~
- 675 [Ayazpour, Z., Sun, K., Zhang, R., and Shen, H.: Evaluation of the directional derivative](#)
676 [approach for timely and accurate satellite - based emission estimation using chemical](#)
677 [transport model simulation of nitrogen oxides, *J. Geophys. Res.*, 130, e2024JD042817,](#)
678 <https://doi.org/10.1029/2024jd042817>, 2025..
- 679 Azouz, N., Drouet, J.-L., Beekmann, M., Siour, G., Wichink Kruit, R., and Cellier, P.:
680 Comparison of spatial patterns of ammonia concentration and dry deposition flux
681 between a regional Eulerian chemistry-transport model and a local Gaussian plume
682 model, *Air Qual. Atmos. Health*, 12, 719–729, <https://doi.org/10.1007/s11869-019-00691-y>, 2019.
- 683
- 684 Behera, S. N. and Sharma, M.: Investigating the potential role of ammonia in ion chemistry of
685 fine particulate matter formation for an urban environment, *Sci. Total Environ.*, 408,
686 3569–3575, <https://doi.org/10.1016/j.scitotenv.2010.04.017>, 2010.
- 687 Beirle, S., Borger, C., Dörner, S., Li, A., Hu, Z., Liu, F., Wang, Y., and Wagner, T.: Pinpointing
688 nitrogen oxide emissions from space, *Sci Adv*, 5, eaax9800,
689 <https://doi.org/10.1126/sciadv.aax9800>, 2019.
- 690 Beirle, S., Borger, C., Dörner, S., Eskes, H., Kumar, V., de Laat, A., and Wagner, T.: Catalog
691 of NOx emissions from point sources as derived from the divergence of the NO2 flux for
692 TROPOMI, *Earth Syst. Sci. Data*, 13, 2995–3012, <https://doi.org/10.5194/essd-13-2995-2021>, 2021.
- 693
- 694 [Blanes-Vidal, V., Hansen, M. N., Pedersen, S., and Rom, H. B.: Emissions of ammonia,](#)
695 [methane and nitrous oxide from pig houses and slurry: Effects of rooting material, animal](#)
696 [activity and ventilation flow, *Agric. Ecosyst. Environ.*, 124, 237–244,](#)
697 <https://doi.org/10.1016/j.agee.2007.10.002>, 2008.
- 698 Bouwman, A. F., Lee, D. S., Asman, W. A. H., Dentener, F. J., Van Der Hoek, K. W., and
699 Olivier, J. G. J.: A global high-resolution emission inventory for ammonia, *Global*
700 *Biogeochem. Cycles*, 11, 561–587, <https://doi.org/10.1029/97gb02266>, 1997.
- 701 van Breemen, N., Burrough, P. A., Velthorst, E. J., van Dobben, H. F., de Wit, T., Ridder, T.
702 B., and Reijnders, H. F. R.: Soil acidification from atmospheric ammonium sulphate in
703 forest canopy throughfall, *Nature*, 299, 548–550, <https://doi.org/10.1038/299548a0>,
704 1982.

- 705 Byrne, B., Liu, J., Bowman, K. W., Pascolini-Campbell, M., Chatterjee, A., Pandey, S.,
706 Miyazaki, K., van der Werf, G. R., Wunch, D., Wennberg, P. O., Roehl, C. M., and Sinha,
707 S.: Carbon emissions from the 2023 Canadian wildfires, *Nature*, 633, 835–839,
708 <https://doi.org/10.1038/s41586-024-07878-z>, 2024.
- 709 Cao, H., Henze, D. K., Shephard, M. W., Dammers, E., Cady-Pereira, K., Alvarado, M.,
710 Lonsdale, C., Luo, G., Yu, F., Zhu, L., Danielson, C. G., and Edgerton, E. S.: Inverse
711 modeling of NH₃ sources using CrIS remote sensing measurements, *Environ. Res. Lett.*,
712 15, 104082, <https://doi.org/10.1088/1748-9326/abb5cc>, 2020.
- 713 Cao, H., Henze, D. K., Zhu, L., Shephard, M. W., Cady-Pereira, K., Dammers, E., Sitwell, M.,
714 Heath, N., Lonsdale, C., Bash, J. O., Miyazaki, K., Flechard, C., Fauvel, Y., Kruit, R. W.,
715 Feigenspan, S., Brümmer, C., Schrader, F., Twigg, M. M., Leeson, S., Tang, Y. S.,
716 Stephens, A. C. M., Braban, C., Vincent, K., Meier, M., Seidler, E., Geels, C., Ellermann,
717 T., Sanocka, A., and Capps, S. L.: 4D-Var inversion of European NH₃ emissions using
718 CrIS NH₃ measurements and GEOS-chem adjoint with bi-directional and uni-directional
719 flux schemes, *J. Geophys. Res.*, 127, e2021JD035687,
720 <https://doi.org/10.1029/2021JD035687>, 2022.
- 721 Chang, Y., Zou, Z., Deng, C., Huang, K., Collett, J. L., Lin, J., and Zhuang, G.: The importance
722 of vehicle emissions as a source of atmospheric ammonia in the megacity of Shanghai,
723 *Atmos. Chem. Phys.*, 16, 3577–3594, <https://doi.org/10.5194/acp-16-3577-2016>, 2016.
- 724 [Chen, Y., Han, Y., Jin, X., and Weng, F.: Assessment of S-NPP CrIS Spectral Calibration](#)
725 [Accuracy and Stability, the 94 th AMS Annual Meeting, 2014.](#)
- 726 Chen, Y., Shen, H., Kaiser, J., Hu, Y., Capps, S. L., Zhao, S., Hakami, A., Shih, J.-S., Pavur,
727 G. K., Turner, M. D., Henze, D. K., Resler, J., Nenes, A., Napelenok, S. L., Bash, J. O.,
728 Fahey, K. M., Carmichael, G. R., Chai, T., Clarisse, L., Coheur, P.-F., Van Damme, M.,
729 and Russell, A. G.: High-resolution hybrid inversion of IASI ammonia columns to
730 constrain US ammonia emissions using the CMAQ adjoint model, *Atmos. Chem. Phys.*,
731 21, 2067–2082, <https://doi.org/10.5194/acp-21-2067-2021>, 2021.
- 732 [Chen, Y., Shen, H., Kaiser, J., Hu, Y., Capps, S. L., Zhao, S., Hakami, A., Shih, J.-S., Pavur,](#)
733 [G. K., Turner, M. D., Henze, D. K., Resler, J., Nenes, A., Napelenok, S. L., Bash, J. O.,](#)
734 [Fahey, K. M., Carmichael, G. R., Chai, T., Clarisse, L., Coheur, P.-F., Van Damme, M.,](#)
735 [and Russell, A. G.: High-resolution hybrid inversion of IASI ammonia columns to](#)
736 [constrain US ammonia emissions using the CMAQ adjoint model, Atmos. Chem. Phys.,](#)
737 [21, 2067–2082, https://doi.org/10.5194/acp-21-2067-2021, 2021.](#)
- 738 Clarisse, L., Shephard, M. W., Dentener, F., Hurtmans, D., Cady-Pereira, K., Karagulian, F.,
739 Van Damme, M., Clerbaux, C., and Coheur, P.-F.: Satellite monitoring of ammonia: A
740 case study of the San Joaquin Valley, *Journal of Geophysical Research: Atmospheres*,
741 115, <https://doi.org/10.1029/2009JD013291>, 2010.
- 742 Clarisse, L., Van Damme, M., and Coheur, P.-F.: Standard daily IASI/Metop-A ULB-LATMOS
743 ammonia (NH₃) L2 product (total column), <https://doi.org/10.25326/10>, 2018.
- 744 Clarisse, L., Franco, B., Van Damme, M., Di Gioacchino, T., Hadji-Lazarou, J., Whitburn, S.,
745 Noppen, L., Hurtmans, D., Clerbaux, C., and Coheur, P.: The IASI NH 3 version 4
746 product: averaging kernels and improved consistency, *Atmos. Meas. Tech.*, 16, 5009–
747 5028, <https://doi.org/10.5194/amt-16-5009-2023>, 2023.

- 748 Clerbaux, C., Boynard, A., Clarisse, L., George, M., Hadji-Lazaro, J., Herbin, H., Hurtmans,
749 D., Pommier, M., Razavi, A., Turquety, S., Wespes, C., and Coheur, P.: Monitoring of
750 atmospheric composition using the thermal infrared IASI/METOP sounder, *Atmos.*
751 *Chem. Phys.*, 9, 6041–6054, <https://doi.org/10.5194/ACP-9-6041-2009>, 2009.
- 752 Dammers, E., McLinden, C., Griffin, D., Shephard, M. W., Van Der Graaf, S., Lutsch, E.,
753 Schaap, M., Gainairu-Matz, Y., Fioletov, V. E., Van Damme, M., Whitburn, S., Clarisse,
754 L., Cady-Pereira, K. E., Clerbaux, C., Coheur, P. F., and Willem Erisman, J., NH3
755 emissions from large point sources derived from CrIS and IASI satellite observations,
756 *Atmos. Chem. Phys.*, 19, 12261–12293, <https://doi.org/10.5194/acp-19-12261-2019>,
757 2019.
- 758 [Dammers, E., Palm, M., Van Damme, M., Vigouroux, C., Smale, D., Conway, S., Toon, G. C.,
759 Jones, N., Nussbaumer, E., Warneke, T., Petri, C., Clarisse, L., Clerbaux, C., Hermans,
760 C., Lutsch, E., Strong, K., Hannigan, J. W., Nakajima, H., Morino, I., Herrera, B.,
761 Stremme, W., Grutter, M., Schaap, M., Wichink Kruit, R. J., Notholt, J., Coheur, P.-F.,
762 and Erisman, J. W.: An evaluation of IASI-NH3 with ground-based Fourier transform
763 infrared spectroscopy measurements, *Atmos. Chem. Phys.*, 16, 10351–10368,
764 <https://doi.org/10.5194/acp-16-10351-2016>, 2016.](https://doi.org/10.5194/acp-16-10351-2016)
- 765 Dammers, E., Shephard, M. W., Palm, M., Cady-Pereira, K., Capps, S., Lutsch, E., Strong, K.,
766 Hannigan, J. W., Ortega, I., Toon, G. C., Stremme, W., Grutter, M., Jones, N., Smale,
767 D., Siemons, J., Hrpcek, K., Tremblay, D., Schaap, M., Notholt, J., and Erisman, J. W.:
768 Validation of the CrIS fast physical NH3 retrieval with ground-based FTIR, *Atmos. Meas.*
769 *Tech.*, 10, 2645–2667, <https://doi.org/10.5194/amt-10-2645-2017>, 2017.
- 770 Dentener, F. J. and Crutzen, P. J.: A three-dimensional model of the global ammonia cycle, *J.*
771 *Atmos. Chem.*, 19, 331–369, <https://doi.org/10.1007/bf00694492>, 1994.
- 772 [Ellis, R. A., Jacob, D. J., Sulprizio, M. P., Zhang, L., Holmes, C. D., Schichtel, B. A.,
773 Blett, T., Porter, E., Pardo, L. H., and Lynch, J. A.: Present and future nitrogen
774 deposition to national parks in the United States: critical load exceedances,
775 *Atmos. Chem. Phys.*, 13, 9083–9095, <https://doi.org/10.5194/acp-13-9083-2013>,
776 2013.](https://doi.org/10.5194/acp-13-9083-2013)
- 777 Erisman, J. W., Galloway, J. N., Seitzinger, S., Bleeker, A., Dise, N. B., Petrescu, A. M. R.,
778 Leach, A. M., and de Vries, W.: Consequences of human modification of the global
779 nitrogen cycle, *Philos. Trans. R. Soc. Lond. B Biol. Sci.*, 368, 20130116,
780 <https://doi.org/10.1098/rstb.2013.0116>, 2013.
- 781 Evangeliou, N., Balkanski, Y., Eckhardt, S., Cozic, A., Van Damme, M., Coheur, P.-F.,
782 Clarisse, L., Shephard, M. W., Cady-Pereira, K. E., and Hauglustaine, D.: 10-year
783 satellite-constrained fluxes of ammonia improve performance of chemistry transport
784 models, *Atmos. Chem. Phys.*, 21, 4431–4451, <https://doi.org/10.5194/acp-21-4431-2021>
785 202110.5194/acp-21-4431-2021-supplement, 2021.
- 786 Galloway, J. N., Aber, J. D., Erisman, J. W., Seitzinger, S. P., Howarth, R. W., Cowling, E. B.,
787 and Cosby, B. J.: The nitrogen cascade, *Bioscience*, 53, 341,
788 [https://doi.org/10.1641/0006-3568\(2003\)053\[0341:tnc\]2.0.co;2](https://doi.org/10.1641/0006-3568(2003)053[0341:tnc]2.0.co;2), 2003.
- 789 Galloway, J. N., Dentener, F. J., Capone, D. G., Boyer, E. W., Howarth, R. W., Seitzinger, S.
790 P., Asner, G. P., Cleveland, C. C., Green, P. A., Holland, E. A., Karl, D. M., Michaels, A.
791 F., Porter, J. H., Townsend, A. R., and Vöösmary, C. J.: Nitrogen cycles: Past, present,

- 792 and future, *Biogeochemistry*, 70, 153–226, <https://doi.org/10.1007/s10533-004-0370-0>,
793 2004.
- 794 Goldberg, D. L., Harkey, M., de Foy, B., Judd, L., Johnson, J., Yarwood, G., and Holloway, T.:
795 Evaluating NO_x emissions and their effect on O₃ production in Texas using TROPOMI
796 NO₂ and HCHO, *Atmos. Chem. Phys.*, 22, 10875–10900, [https://doi.org/10.5194/acp-](https://doi.org/10.5194/acp-22-10875-2022)
797 22-10875-2022, 2022.
- 798 Gong, C., Tian, H., Liao, H., Pan, N., Pan, S., Ito, A., Jain, A. K., Kou-Giesbrecht, S., Joos, F.,
799 Sun, Q., Shi, H., Vuichard, N., Zhu, Q., Peng, C., Maggi, F., Tang, F. H. M., and Zaehle,
800 S.: Global net climate effects of anthropogenic reactive nitrogen, *Nature*, 632, 557–563,
801 <https://doi.org/10.1038/s41586-024-07714-4>, 2024.
- 802 Gu, B., Zhang, L., Van Dingenen, R., Vieno, M., Van Grinsven, H. J., Zhang, X., Zhang, S.,
803 Chen, Y., Wang, S., Ren, C., Rao, S., Holland, M., Winiwarter, W., Chen, D., Xu, J., and
804 Sutton, M. A.: Abating ammonia is more cost-effective than nitrogen oxides for mitigating
805 PM_{2.5} air pollution, *Science*, 374, 758–762, <https://doi.org/10.1126/science.abf8623>,
806 2021.
- 807 Heil, G. W. and Diemont, W. H.: Raised nutrient levels change heathland into grassland,
808 *Vegetatio*, 53, 113–120, <https://doi.org/10.1007/bf00043031>, 1983.
- 809 Hersbach, H., Bell, B., Berrisford, P., Hirahara, S., Horányi, A., Muñoz-Sabater, J., Nicolas, J.,
810 Peubey, C., Radu, R., Schepers, D., Simmons, A., Soci, C., Abdalla, S., Abellan, X.,
811 Balsamo, G., Bechtold, P., Biavati, G., Bidlot, J., Bonavita, M., De Chiara, G., Dahlgren,
812 P., Dee, D., Diamantakis, M., Dragani, R., Flemming, J., Forbes, R., Fuentes, M., Geer,
813 A., Haimberger, L., Healy, S., Hogan, R. J., Hólm, E., Janisková, M., Keeley, S.,
814 Laloyaux, P., Lopez, P., Lupu, C., Radnoti, G., de Rosnay, P., Rozum, I., Vamborg, F.,
815 Villaume, S., and Jean-Noël Thépaut: The ERA5 global reanalysis, *Quart. J. Roy.
816 Meteor. Soc.*, 146, 1999–2049, <https://doi.org/10.1002/qj.3803>, 2020.
- 817 Hersbach, H., Bell, B., Berrisford, P., Biavati, G., Horányi, A., Muñoz-Sabater, J., Nicolas, J.,
818 Peubey, C., Radu, R., Rozum, I., Schepers, D., Simmons, A., Soci, C., Dee, D., and
819 Thépaut, J.-N.: ERA5 hourly data on single levels from 1940 to present,
820 <https://doi.org/10.24381/CDS.ADBB2D47>, 2023.
- 821 Hesterberg, R., Blatter, A., Fahrni, M., Rosset, M., Neftel, A., Eugster, W., and Wanner, H.:
822 Deposition of nitrogen-containing compounds to an extensively managed grassland in
823 central Switzerland, *Environ. Pollut.*, 91, 21–34, [https://doi.org/10.1016/0269-](https://doi.org/10.1016/0269-7491(95)00036-q)
824 7491(95)00036-q, 1996.
- 825 Hu, C., Griffis, T. J., Frie, A., Baker, J. M., Wood, J. D., Millet, D. B., Yu, Z., Yu, X., and
826 Czarnetzki, A. C.: A multiyear constraint on ammonia emissions and deposition within
827 the US corn belt, *Geophys. Res. Lett.*, 48, e2020GL090865,
828 <https://doi.org/10.1029/2020gl090865>, 2021.
- 829 Kharol, S. K., Shephard, M. W., McLinden, C. A., Zhang, L., Sioris, C. E., O'Brien, J. M., Vet,
830 R., Cady-Pereira, K. E., Hare, E., Siemons, J., and Krotkov, N. A.: Dry deposition of
831 reactive nitrogen from satellite observations of ammonia and nitrogen dioxide over north
832 America, *Geophys. Res. Lett.*, 45, 1157–1166, <https://doi.org/10.1002/2017gl075832>,
833 2018.
- 834 Kirchner, M., Jakobi, G., Feicht, E., Bernhardt, M., and Fischer, A.: Elevated NH₃ and NO₂ air

835 concentrations and nitrogen deposition rates in the vicinity of a highway in Southern
836 Bavaria, *Atmos. Environ.* (1994), 39, 4531–4542,
837 <https://doi.org/10.1016/j.atmosenv.2005.03.052>, 2005.

838 Krupa, S. V.: Effects of atmospheric ammonia (NH₃) on terrestrial vegetation: a review,
839 *Environ. Pollut.*, 124, 179–221, [https://doi.org/10.1016/s0269-7491\(02\)00434-7](https://doi.org/10.1016/s0269-7491(02)00434-7), 2003.

840 Lin, H., Jacob, D. J., Lundgren, E. W., Sulprizio, M. P., Keller, C. A., Fritz, T. M., Eastham, S.
841 D., Emmons, L. K., Campbell, P. C., Baker, B., Saylor, R. D., and Montuoro, R.:
842 Harmonized Emissions Component (HEMCO) 3.0 as a versatile emissions component
843 for atmospheric models: application in the GEOS-Chem, NASA GEOS, WRF-GC,
844 CESM2, NOAA GEFS-Aerosol, and NOAA UFS models, *Geosci. Model Dev.*, 14, 5487–
845 5506, <https://doi.org/10.5194/gmd-14-5487-2021>, 2021.

846 Liu, L., Zhang, X., Wong, A. Y. H., Xu, W., Liu, X., Li, Y., Mi, H., Lu, X., Zhao, L., Wang, Z.,
847 Wu, X., and Wei, J.: Estimating global surface ammonia concentrations inferred from
848 satellite retrievals, *Atmos. Chem. Phys.*, 19, 12051–12066, <https://doi.org/10.5194/acp-19-12051-2019>, 2019.

850 Liu, L., Xu, W., Lu, X., Zhong, B., Guo, Y., Lu, X., Zhao, Y., He, W., Wang, S., Zhang, X., Liu,
851 X., and Vitousek, P.: Exploring global changes in agricultural ammonia emissions and
852 their contribution to nitrogen deposition since 1980, *Proc. Natl. Acad. Sci. U. S. A.*, 119,
853 e2121998119, <https://doi.org/10.1073/pnas.2121998119>, 2022.

854 Li, Y., Schichtel, B. A., Walker, J. T., Schwede, D. B., Chen, X., Lehmann, C. M. B., Puchalski,
855 M. A., Gay, D. A., and Collett, J. L., Jr: Increasing importance of deposition of reduced
856 nitrogen in the United States, *Proc. Natl. Acad. Sci. U. S. A.*, 113, 5874–5879,
857 <https://doi.org/10.1073/pnas.1525736113>, 2016.

858 Lonsdale, C. R. and Sun, K.: Nitrogen oxides emissions from selected cities in North America,
859 Europe, and East Asia observed by the Tropospheric Monitoring Instrument
860 (TROPOMI) before and after the COVID-19 pandemic, *Atmos. Chem. Phys.*, 23, 8727–
861 8748, <https://doi.org/10.5194/acp-23-8727-2023>, 2023.

862 Loubet, B., Asman, W. A. H., Theobald, M. R., Hertel, O., Tang, Y. S., Robin, P., Hassouna,
863 M., Dämmgen, U., Genermont, S., Cellier, P., and Sutton, M. A.: Ammonia deposition
864 near hot spots: Processes, models and monitoring methods, in: *Atmospheric Ammonia*,
865 Springer Netherlands, Dordrecht, 205–267, https://doi.org/10.1007/978-1-4020-9121-6_15, 2009.

867 Luo, Z., Zhang, Y., Chen, W., Van Damme, M., Coheur, P.-F., and Clarisse, L.: Estimating
868 global ammonia (NH₃) emissions based on IASI observations from 2008 to 2018, *Atmos.*
869 *Chem. Phys.*, 22, 10375–10388, <https://doi.org/10.5194/acp-22-10375-2022>, 2022.

870 Ma, R., Li, K., Guo, Y., Zhang, B., Zhao, X., Linder, S., Guan, C., Chen, G., Gan, Y., and Meng,
871 J.: Mitigation potential of global ammonia emissions and related health impacts in the
872 trade network, *Nat. Commun.*, 12, 6308, <https://doi.org/10.1038/s41467-021-25854-3>,
873 2021.

874 Marais, E. A., Pandey, A. K., Van Damme, M., Clarisse, L., Coheur, P.-F., Shephard, M. W.,
875 Cady-Pereira, K. E., Misselbrook, T., Zhu, L., Luo, G., and Yu, F.: UK ammonia
876 emissions estimated with satellite observations and GEOS-chem, *J. Geophys. Res.*,
877 126, <https://doi.org/10.1029/2021jd035237>, 2021.

- 878 Nelson, A. J., Koloutsou-Vakakis, S., Rood, M. J., Myles, L., Lehmann, C., Bernacchi, C.,
879 Balasubramanian, S., Joo, E., Heuer, M., Vieira-Filho, M., and Lin, J.: Season-long
880 ammonia flux measurements above fertilized corn in central Illinois, USA, using relaxed
881 eddy accumulation, *Agric. For. Meteorol.*, 239, 202–212,
882 <https://doi.org/10.1016/j.agrformet.2017.03.010>, 2017.
- 883 Pan, D., Benedict, K. B., Golston, L. M., Wang, R., Collett, J. L., Jr, Tao, L., Sun, K., Guo, X.,
884 Ham, J., Prenni, A. J., Schichtel, B. A., Mikoviny, T., Müller, M., Wisthaler, A., and
885 Zondlo, M. A.: Ammonia dry deposition in an alpine ecosystem traced to agricultural
886 emission hotspots, *Environ. Sci. Technol.*, 55, 7776–7785,
887 <https://doi.org/10.1021/acs.est.0c05749>, 2021.
- 888 Pan, D., Mauzerall, D. L., Wang, R., Guo, X., Puchalski, M., Guo, Y., Song, S., Tong, D.,
889 Sullivan, A. P., Schichtel, B. A., Collett, J. L., Jr, and Zondlo, M. A.: Regime shift in
890 secondary inorganic aerosol formation and nitrogen deposition in the rural United States,
891 *Nat. Geosci.*, 17, 617–623, <https://doi.org/10.1038/s41561-024-01455-9>, 2024.
- 892 Pearson, J. and Stewart, G. R.: The deposition of atmospheric ammonia and its effects on
893 plants, *New Phytol.*, 125, 283–305, <https://doi.org/10.1111/j.1469-8137.1993.tb03882.x>,
894 1993.
- 895 Reche, C., Viana, M., Karanasiou, A., Cusack, M., Alastuey, A., Artiñano, B., Revuelta, M. A.,
896 López-Mahía, P., Blanco-Heras, G., Rodríguez, S., Sánchez de la Campa, A. M.,
897 Fernández-Camacho, R., González-Castanedo, Y., Mantilla, E., Tang, Y. S., and
898 Querol, X.: Urban NH₃ levels and sources in six major Spanish cities, *Chemosphere*,
899 119, 769–777, <https://doi.org/10.1016/j.chemosphere.2014.07.097>, 2015.
- 900 Shephard, M. W. and Cady-Pereira, K.E.: Cross-track Infrared Sounder (CrIS) Satellite
901 Observations of Tropospheric Ammonia, *Atmos. Meas. Tech.*, 8, 1323–1336,
902 <https://doi.org/10.5194/amt-8-1323-2015>, 2015.
- 903 Shephard, M. W., Dammers, E., Cady-Pereira, K. E., Kharol, S. K., Thompson, J., Gainariu-
904 Matz, Y., Zhang, J., McLinden, C. A., Kovachik, A., Moran, M., Bittman, S., Sioris, C. E.,
905 Griffin, D., Alvarado, M. J., Lonsdale, C., Savic-Jovicic, V., and Zheng, Q.: Ammonia
906 measurements from space with the Cross-track Infrared Sounder: characteristics and
907 applications, *Atmos. Chem. Phys.*, 20, 2277–2302, [https://doi.org/10.5194/acp-20-2277-](https://doi.org/10.5194/acp-20-2277-2020)
908 2020, 2020.
- 909 Sitwell, M., Shephard, M. W., Rochon, Y., Cady-Pereira, K., and Dammers, E.: An ensemble-
910 variational inversion system for the estimation of ammonia emissions using CrIS satellite
911 ammonia retrievals, *Atmos. Chem. Phys.*, 22, 6595–6624, [https://doi.org/10.5194/acp-](https://doi.org/10.5194/acp-22-6595-2022)
912 22-6595-2022, 2022.
- 913 [Sommer, S. G., Olesen, J. E., and Christensen, B. T.: Effects of temperature, wind speed and](#)
914 [air humidity on ammonia volatilization from surface applied cattle slurry, *J. Agric. Sci.*,](#)
915 [117, 91–100, <https://doi.org/10.1017/S0021859600079016>, 1991.](#)
- 916 Sun, K.: Derivation of emissions from satellite-observed column amounts and its application
917 to TROPOMI NO₂ and CO observations, *Geophys. Res. Lett.*, 49,
918 <https://doi.org/10.1029/2022gl101102>, 2022.
- 919 Sun, K., Tao, L., Miller, D. J., Pan, D., Golston, L. M., Zondlo, M. A., Griffin, R. J., Wallace, H.
920 W., Leong, Y. J., Yang, M. M., Zhang, Y., Mauzerall, D. L., and Zhu, T.: Vehicle

- 921 emissions as an important urban ammonia source in the United States and China,
922 *Environ. Sci. Technol.*, 51, 2472–2481, <https://doi.org/10.1021/acs.est.6b02805>, 2017.
- 923 Sun, K., Zhu, L., Cady-Pereira, K., Chan Miller, C., Chance, K., Clarisse, L., Coheur, P.-F.,
924 González Abad, G., Huang, G., Liu, X., Van Damme, M., Yang, K., and Zondlo, M.: A
925 physics-based approach to oversample multi-satellite, multispecies observations to a
926 common grid, *Atmos. Meas. Tech.*, 11, 6679–6701, [https://doi.org/10.5194/amt-11-](https://doi.org/10.5194/amt-11-6679-2018)
927 6679-2018, 2018.
- 928 Sutton, M., Reis, S., and Baker, S. (Eds.): *Atmospheric Ammonia: Detecting emission changes*
929 *and environmental impacts. Results of an Expert Workshop under the Convention on*
930 *Long-range Transboundary Air Pollution*, 1st ed., Springer, New York, NY, 464 pp.,
931 <https://doi.org/10.1007/978-1-4020-9121-6>, 2009.
- 932 Sutton, M. A., Erisman, J. W., Dentener, F., and Möller, D.: Ammonia in the environment: from
933 ancient times to the present, *Environ. Pollut.*, 156, 583–604,
934 <https://doi.org/10.1016/j.envpol.2008.03.013>, 2008.
- 935 Sutton, M. A., Reis, S., Riddick, S. N., Dragosits, U., Nemitz, E., Theobald, M. R., Tang, Y. S.,
936 Braban, C. F., Vieno, M., Dore, A. J., Mitchell, R. F., Wanless, S., Daunt, F., Fowler, D.,
937 Blackall, T. D., Milford, C., Flechard, C. R., Loubet, B., Massad, R., Cellier, P., Personne,
938 E., Coheur, P. F., Clarisse, L., Van Damme, M., Ngadi, Y., Clerbaux, C., Skjøth, C. A.,
939 Geels, C., Hertel, O., Wichink Kruit, R. J., Pinder, R. W., Bash, J. O., Walker, J. T.,
940 Simpson, D., Horváth, L., Misselbrook, T. H., Bleeker, A., Dentener, F., and de Vries,
941 W.: Towards a climate-dependent paradigm of ammonia emission and deposition,
942 *Philos. Trans. R. Soc. Lond. B Biol. Sci.*, 368, 20130166,
943 <https://doi.org/10.1098/rstb.2013.0166>, 2013.
- 944 Sutton, M. A., van Dijk, N., Levy, P. E., Jones, M. R., Leith, I. D., Sheppard, L. J., Leeson, S.,
945 Sim Tang, Y., Stephens, A., Braban, C. F., Dragosits, U., Howard, C. M., Vieno, M.,
946 Fowler, D., Corbett, P., Naikoo, M. I., Munzi, S., Ellis, C. J., Chatterjee, S., Steadman,
947 C. E., Móríng, A., and Wolseley, P. A.: Alkaline air: changing perspectives on nitrogen
948 and air pollution in an ammonia-rich world, *Philos. Trans. A Math. Phys. Eng. Sci.*, 378,
949 20190315, <https://doi.org/10.1098/rsta.2019.0315>, 2020.
- 950 Tang, Y. S., Braban, C. F., Dragosits, U., Dore, A. J., Simmons, I., van Dijk, N., Poskitt, J., Dos
951 Santos Pereira, G., Keenan, P. O., Conolly, C., Vincent, K., Smith, R. I., Heal, M. R., and
952 Sutton, M. A.: Drivers for spatial, temporal and long-term trends in atmospheric ammonia
953 and ammonium in the UK, *Atmos. Chem. Phys.*, 18, 705–733,
954 <https://doi.org/10.5194/acp-18-705-2018>, 2018.
- 955 Tian, H., Xu, R., Canadell, J. G., Thompson, R. L., Winiwarter, W., Suntharalingam, P.,
956 Davidson, E. A., Ciais, P., Jackson, R. B., Janssens-Maenhout, G., Prather, M. J.,
957 Regnier, P., Pan, N., Pan, S., Peters, G. P., Shi, H., Tubiello, F. N., Zaehle, S., Zhou, F.,
958 Arneeth, A., Battaglia, G., Berthet, S., Bopp, L., Bouwman, A. F., Buitenhuis, E. T., Chang,
959 J., Chipperfield, M. P., Dangal, S. R. S., Dlugokencky, E., Elkins, J. W., Eyre, B. D., Fu,
960 B., Hall, B., Ito, A., Joos, F., Krummel, P. B., Landolfi, A., Laruelle, G. G., Lauerwald, R.,
961 Li, W., Lienert, S., Maavara, T., MacLeod, M., Millet, D. B., Olin, S., Patra, P. K., Prinn,
962 R. G., Raymond, P. A., Ruiz, D. J., van der Werf, G. R., Vuichard, N., Wang, J., Weiss,
963 R. F., Wells, K. C., Wilson, C., Yang, J., and Yao, Y.: A comprehensive quantification of
964 global nitrous oxide sources and sinks, *Nature*, 586, 248–256,
965 <https://doi.org/10.1038/s41586-020-2780-0>, 2020.

- 966 [Van Damme, M., Clarisse, L., Heald, C. L., Hurtmans, D., Ngadi, Y., Clerbaux, C., Dolman, A.](#)
967 [J., Erisman, J. W., and Coheur, P. F.: Global distributions, time series and error](#)
968 [characterization of atmospheric ammonia \(NH₃\) from IASI satellite observations, *Atmos.*](#)
969 [Chem. Phys., 14, 2905–2922, <https://doi.org/10.5194/acp-14-2905-2014>, 2014.](#)
- 970 [Van Damme, M., Clarisse, L., Dammers, E., Liu, X., Nowak, J. B., Clerbaux, C., Flechard, C.](#)
971 [R., Galy-Lacaux, C., Xu, W., Neuman, J. A., Tang, Y. S., Sutton, M. A., Erisman, J. W.,](#)
972 [and Coheur, P. F.: Towards validation of ammonia \(NH₃\) measurements from the IASI](#)
973 [satellite, *Atmos. Meas. Tech.*, 8, 1575–1591, <https://doi.org/10.5194/amt-8-1575-2015>,](#)
974 [2015.](#)
- 975 Van Damme, M., Clarisse, L., Whitburn, S., Hadji-Lazaro, J., Hurtmans, D., Clerbaux, C., and
976 Coheur, P.-F.: Industrial and agricultural ammonia point sources exposed, *Nature*, 564,
977 99–103, <https://doi.org/10.1038/s41586-018-0747-1>, 2018.
- 978 Vira, J., Hess, P., Ossouhou, M., and Galy-Lacaux, C.: Evaluation of interactive and prescribed
979 agricultural ammonia emissions for simulating atmospheric composition in CAM-chem,
980 *Atmos. Chem. Phys.*, 22, 1883–1904, <https://doi.org/10.5194/acp-22-1883-2022>, 2022.
- 981 Wang, R., Guo, X., Pan, D., Kelly, J. T., Bash, J. O., Sun, K., Paulot, F., Clarisse, L., Van
982 Damme, M., Whitburn, S., Coheur, P.-F., Clerbaux, C., and Zondlo, M. A.: Monthly
983 patterns of ammonia over the contiguous United States at 2-km resolution, *Geophys.*
984 *Res. Lett.*, 48, <https://doi.org/10.1029/2020gl090579>, 2021.
- 985 Wang, R., Pan, D., Guo, X., Sun, K., Clarisse, L., Van Damme, M., Coheur, P.-F., Clerbaux,
986 C., Puchalski, M., and Zondlo, M. A.: Bridging the spatial gaps of the Ammonia
987 Monitoring Network using satellite ammonia measurements, *Atmos. Chem. Phys.*, 23,
988 13217–13234, <https://doi.org/10.5194/acp-23-13217-2023>, 2023.
- 989 Wang, S., Nan, J., Shi, C., Fu, Q., Gao, S., Wang, D., Cui, H., Saiz-Lopez, A., and Zhou, B.:
990 Atmospheric ammonia and its impacts on regional air quality over the megacity of
991 Shanghai, China, *Sci. Rep.*, 5, 15842, <https://doi.org/10.1038/srep15842>, 2015.
- 992 Warner, J. X., Dickerson, R. R., Wei, Z., Strow, L. L., Wang, Y., and Liang, Q.: Increased
993 atmospheric ammonia over the world's major agricultural areas detected from space:
994 Global Atmospheric NH₃14 Year Trends, *Geophys. Res. Lett.*, 44, 2875–2884,
995 <https://doi.org/10.1002/2016GL072305>, 2017.
- 996 Zhang, L., Jacob, D. J., Knipping, E. M., Kumar, N., Munger, J. W., Carouge, C. C., van
997 Donkelaar, A., Wang, Y. X., and Chen, D.: Nitrogen deposition to the United States:
998 distribution, sources, and processes, *Atmos. Chem. Phys.*, 12, 4539–4554,
999 <https://doi.org/10.5194/acp-12-4539-2012>, 2012.
- 1000 Zhang, L., Chen, Y., Zhao, Y., Henze, D. K., Zhu, L., Song, Y., Paulot, F., Liu, X., Pan, Y., Lin,
1001 Y., and Huang, B.: Agricultural ammonia emissions in China: reconciling bottom-up and
1002 top-down estimates, *Atmos. Chem. Phys.*, 18, 339–355, [https://doi.org/10.5194/acp-18-](https://doi.org/10.5194/acp-18-339-2018)
1003 [339-2018](#), 2018.
- 1004 Zhu, L., Henze, D. K., Cady-Pereira, K. E., Shephard, M. W., Luo, M., Pinder, R. W., Bash, J.
1005 O., and Jeong, G.-R.: Constraining U.S. ammonia emissions using TES remote sensing
1006 observations and the GEOS-Chem adjoint model: INVERSE MODELING OF
1007 NH₃EMISSIONS, *J. Geophys. Res.*, 118, 3355–3368,
1008 <https://doi.org/10.1002/jgrd.50166>, 2013.